UNIVERSITÀ DEGLI STUDI DI PISA

Dipartimento di Fisica

Master Thesis

Investigation on a two-frequency Paul trap for a cavity optomechanics system

Candidato

Lorenzo Dania

Relatori

Prof. Tracy E. Northup

Prof. Francesco Fuso

ANNO ACCADEMICO 2016-2017

Contents

Introduction **7**

1 Cavity optomechanics with levitated nanoparticles **11**

1.1 The optomechanical coupling 11

Optical cavity 11

Coupling of a dielectric and a cavity field 13

1.2 Cavity optomechanics assisted by a qubit 17

2 Paul trap theory **21**

2.1 The linear Paul trap theory 22

2.1.1 The effect of damping on the stability diagrams 30

2.2 Paul trap driven by two frequencies 31

2.2.1 Trapping two particles with one frequency 35

2.2.2 Trapping two particles with two frequencies 36

2.3 Paul trap as a mass spectrometer 37

3 Experimental apparatus **39**

3.1 The linear Paul trap realization 39

3.1.1 Design and fabrication 39

3.1.2 Driving the trap 43

3.2 Particle preparation and loading methods 44

3.2.1 Electrospray ionization of nanoparticles 45

3.2.2 Charging and launching of microparticles 46

3.3 Detection schemes 47

3.3.1 Laser and spatial filter 48

3.3.2 Back-focal-plane interferometry detection . . . 48
3.3.3 Camera detection . . . 55
3.4 Data analysis tool . . . 57

4 Experimental results **59**
4.1 Characterization of the trap and loading methods . . . 59
4.1.1 Charge over mass measurements . . . 60
4.2 Stability diagrams . . . 62
4.2.1 Stability diagram of the microparticle . . . 64
4.2.2 Stability diagram of the nanoparticle . . . 65
4.3 Power spectral density of particle motion . . . 66
4.3.1 Overdamped regime of the equation of motion . . . 67
4.3.2 PSD of microparticle . . . 68
4.3.3 PSD of nanoparticle . . . 70
4.4 Two-particle results . . . 72
4.4.1 Second particle loading . . . 72
4.4.2 PSDs of particle motion . . . 74

Conclusions and outlook **77**
Summary . . . 77
Next step: loading nanospheres in vacuum . . . 78

Appendices **79**

A Numerical code for the stability diagrams **80**

Bibliography **83**

Introduction

Light can transfer momentum to a mechanical oscillator via the radiation pressure force. Conversely, the mechanical oscillator can act back on the reflected light field, modifying its frequency and amplitude. This dynamical back-action can be enhanced by the use of an optical cavity, where the optical interaction is enhanced by every round-trip performed by the photons inside the cavity [1]. This light-matter interaction is at the heart of the field of cavity optomechanics.
Cavity optomechanics has been implemented in a large variety of physical systems, including interferometer's suspended mirrors for gravitational wave detection [2], micromechanical membrane in a superconducting microwave circuit [3], photonic crystal nano beam [4] and cold atoms coupled to an optical cavity [5].
From this plethora of systems, several interesting applications arise, among which quantum control of mesoscopic systems is of particular interest, as well as quantum control of optical fields via mechanics.
To achieve this quantum control, it is necessary to bring the mechanical oscillator to the quantum regime. Then, one must be able to engineer the required quantum interaction. Finally, one must ensure that the mechanical oscillator does not decohere too fast, such that the environment erases the quantum features of the system.
Among the various optomechanical systems that aim at maximizing the decoupling from the thermal environment (decoherence), levitated systems provide superior performance due to the complete suppression of clamping losses. They are therefore ideal candidates to engineer long-lived quantum states [6].

In this thesis research, I took part in setting up from scratch the first levitated optomechanics experiment at the University of Innsbruck, which has the ambitious long-term goal to prepare the center-of-mass position of a nanosphere in a non-classical state of motion.
The system will be formed by a high-finesse optical cavity dispersively coupled to a glass nanosphere trapped in an electrodynamic Paul trap. Moreover, the cavity light field will couple as well to a single calcium ion, whose role will be to engineer non-linear interactions with the motion of the nanosphere [7]. This bold

assumption, however, relies on the feasibility of confining both the nanoparticle and the ion within the same trap.
Paul traps are based on the ponderomotive mean force felt by a charged particle in a quadrupolar time-oscillating electric potential, whose strength is weighted by the charge-to-mass ratio of the trapped particle. As a result, a good trap for an ion will not provide good confinement for a nanosphere, which has a typical charge-to-mass ratio $\sim 10^7$ times larger than that of an ion.

My work has consisted of investigating a novel proposal [8] to use a Paul trap driven by two frequencies in order to confine two species with a very large charge-to-mass difference.
To assess the viability of this approach, we have re-scaled the system, as the relevant quantity is only on the charge-to-mass ratios. We thus used nanometer- and micrometer-size silica spheres instead of ions and nanospheres.
First, a test Paul trap for working in air was designed and built, together with an optical detection system based on interferometric detection of particle motion. Afterwards, the single-particle behavior of both a nano-and a microsphere has been individually characterized, in order to determine the best trap parameters for each particle. Finally, both micro- and nanospheres were successfully trapped with a two-frequencies field.
From a careful analysis of the trap parameters space, however, it resulted that air damping reduced the two frequencies trapping efficiency. In the next future, the same investigations have thus to be carried in a vacuum environment.
The manuscript is divided into four chapters, organized as follows:

- **Chapter 1** Here I introduce the basic concepts of the optomechanical interaction and how this can be used to cool down the center of mass of a mechanical oscillator in the semiclassical regime. Some theoretical elements regarding the role played by the ion (here treated as a two level system, for simplicity) will also be elucidated.

- **Chapter 2** Here the theory of the functioning of a Paul trap is described. In the first section of the chapter, the well-established theory about single-frequency trapping will be shown, while the second section will cover the novel proposal of using two frequencies to optimize the co-trapping of different species with a large charge-to-mass ratio mismatch. Afterwards, the use of a Paul trap as a mass spectrometer will be briefly explained.

- **Chapter 3** This chapter is dedicated to the description of the experimental apparatus used during my

thesis research. Each section describes part of the set-up, namely, the Paul trap, the various loading methods used, and the detection system implemented, together with the data acquisition tools utilized to store and analyze data from the experiment.

- **Chapter 4** This last chapter is devoted to presenting the experimental results that I have obtained in the laboratory. In the first part, a characterization of nano- and microparticles will be given in terms of charge-to-mass measurements and stability performance of the trap. Afterwards, a spectrum analysis of the particles' motion will shed light on the effects of air damping on the trapping mechanism. To conclude, the first results on trapping two species of particles will be presented and discussed.

Chapter 1

Cavity optomechanics with levitated nanoparticles

This chapter will provide a basic theoretical introduction to the field of cavity optomechanics, by means of a system composed of a levitating dielectric nanoparticle dispersively coupled to an optical cavity.
In the first part of this chapter, the optomechanical coupling between a levitated nanosphere and a single cavity mode will be shown.
Afterwards, the total Hamiltonian of the system will be modified by adding a two-level system (a single ion) interacting with the same cavity mode, which will allow the implementation of the nonlinear interactions required to prepare non-Gaussian states.

1.1 The optomechanical coupling

Optical cavity

The simplest picture of an optical cavity consists of two highly reflective mirrors separated by a distance L. This geometrical configuration supports a series of longitudinal electromagnetic resonances, equally separated in frequency by the so-called free spectral range $\Delta\omega_{FSR} = \frac{\pi c}{L}$, where c is the speed of light in vacuum. The intracavity field frequency ω_c has to be an integer multiple of $\Delta\omega_{FSR}$, namely,

$$\omega_c = m\frac{\pi c}{L} \tag{1.1.1}$$

with m an integer.
In order for the cavity to be driven with an external field, one of the two mirrors has to be able to transmit

some light and thus has to be not perfectly reflective, leading to transmission losses of the confined electromagnetic field at a rate κ_{ext}. Moreover, additional losses such as absorption, diffraction and scattering will limit the average lifetime of the photons circulating inside the cavity [9]. These losses are taken into account as an additional contribution (κ_0) to the total decay rate $\kappa = \kappa_{ext} + \kappa_0$.

Cavity equation of motion

A quantum mechanical treatment of the cavity dynamics can be implemented by means of the input-output formalism [10]. Here, the intracavity field oscillating at the cavity frequency w_c is described by the creation and annihilation operators $\hat{a}^\dagger$ and $\hat{a}$.

The equation of motion for a cavity driven by external laser light at frequency ω_L, rotating at the driving laser frequency, is [11]

$$\dot{\hat{a}} = -\frac{\kappa}{2}\hat{a} + i\Delta\hat{a} + \sqrt{\kappa_{ext}}\hat{a}_{in} + \sqrt{\kappa_0}\hat{f}_{in}. \tag{1.1.2}$$

Here, $\Delta = \omega_L - \omega_c$ is the laser detuning, and $\hat{a}_{in}$ represents the creation operator for the field of the input driving laser, which is related to the incoming laser power $P_{in} = \hbar\omega_L\langle\hat{a}_{in}^\dagger\hat{a}_{in}\rangle$, such that $\langle\hat{a}_{in}^\dagger\hat{a}_{in}\rangle$ is the rate at which photons enter the cavity.

The cavity amplitude decays at rate $\kappa/2$, and vacuum fluctuations $\hat{f}_{in}$ drive the cavity from the additional input ports.

The output cavity field (here we are considering only one mirror as the input-output interface of the cavity, see Fig. (1.1)) consists of the reflected driving field interfering with the losses from the intracavity field, fulfilling the boundary condition

$$\hat{a}_{out} = \hat{a}_{in} - \sqrt{\kappa_{ext}}\hat{a}. \tag{1.1.3}$$

Since a typical optomechanics experiment works with a large number of photons inside the cavity, it is worth to consider the steady-state evolution for the classical amplitude $\langle\hat{a}\rangle$. For this purpose, by setting $\dot{\hat{a}} = 0$ in Eq. (1.1.2), we obtain

$$\langle\hat{a}\rangle = \frac{\sqrt{\kappa_{ext}}\langle\hat{a}_{in}\rangle}{\frac{\kappa}{2} - i\Delta} \tag{1.1.4}$$

from which we can calculate the mean intracavity photon number

$$\bar{n} = |\langle\hat{a}\rangle|^2 = \frac{\kappa_{ext}}{\Delta^2 + (\kappa/2)^2}\frac{P_{in}}{\hbar\omega_L}. \tag{1.1.5}$$

Eq. (1.1.5) tells us that the average number of circulating photons and thus the intracavity power depends on the detuning between the cavity and driving laser frequencies $\Delta = \omega_L - \omega_c$.

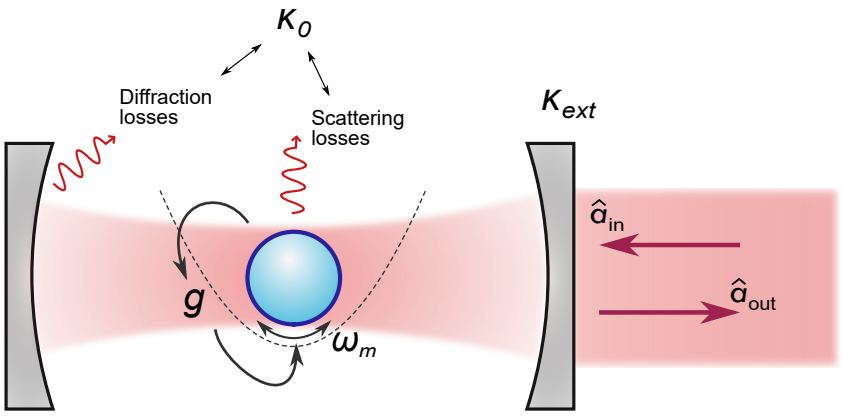

Figure 1.1: Schematic representation of a nanosphere oscillating in its trapping potential at frequency ω_m coupled with the strength g (see text) to an optical cavity. Both the input ($\hat{a}_{in}$) and the output ($\hat{a}_{out}$) light field use the same semi-transparent mirror as coupling interface, which has a loss rate κ_{ext}. Other internal losses, such as scattering as well as diffraction, are grouped together in κ_0.

Coupling of a dielectric and a cavity field

We now consider a system composed of a levitating dielectric particle oscillating in a harmonic potential inside an optical cavity, as sketched in Fig. (1.1). This particle confinement can be realized for example by optical tweezers [12] or by a Paul trap [13], provided the presence of a net charge on the sphere (cf. Chap. 2). At this stage, though, we are only interested in the particle motion as a harmonic oscillator whose center-of-mass position x obeys the classical equation of motion

$$m\ddot{x} + m\Gamma_m\dot{x} + m\omega_m^2 x = F_{ext}, \tag{1.1.6}$$

where ω_m is the mechanical oscillation frequency and Γ_m its energy dissipation rate, and F_{ext} stands for any other external applied force on the oscillator, like thermal fluctuations or an additional optical force (cf. Chap. 4.3.1).

Eq. (1.1.6) can be solved in the frequency space: by introducing the Fourier transform $x(\omega) = \int_{-\infty}^{\infty} dt\, e^{i\omega t} x(t)$, the response $x(\omega)$ to the applied external force $F_{ext}(\omega)$ is given by

$$x(\omega) = \chi(\omega) F_{ext}(\omega) \tag{1.1.7}$$

where the susceptibility χ is defined as

$$\chi(\omega) = \frac{1}{m(\omega_m^2 - \omega^2) - im\Gamma_m\omega}. \tag{1.1.8}$$

At this point, we have described how these two independent harmonic oscillators, one mechanical and one optical, evolve independently. Now, we want to see how, via a dispersive interaction, an optomechanical

coupling arises.

First, we consider the action of the particle on the light field.
When a dielectric object such a SiO_2 glass sphere is placed inside an optical cavity, it increases the effective cavity length due to the higher refractive index of the dielectric medium. As result, the cavity resonance frequency ω_c experiences a shift $\delta\omega_c$ (so that $\omega_c \to \omega_{c0} + \delta\omega_c$, where ω_{c0} is the unperturbed cavity resonance frequency, i.e., in the absence of the particle) that can be calculated with the Bethe-Schwinger formula [14,15] as

$$\frac{\delta\omega_c}{\omega_{c0}} = -\frac{1}{2}\frac{\int d^3\mathbf{r}\delta P(\mathbf{r})\cdot\mathbf{E}(\mathbf{r})}{\int d^3\mathbf{r}\epsilon_0\mathbf{E}^2(\mathbf{r})} \approx -\frac{3V}{4V_c}\frac{(\epsilon-1)}{(\epsilon+2)}\cos(2kx-2\phi), \tag{1.1.9}$$

where $\delta P(\mathbf{r})$ is the variation of the permittivity caused by the presence of the dielectric particle, $\mathbf{E} \propto \cos(\mathbf{kr}-\phi)$ is the bare cavity mode profile ($\mathbf{k}$ being the wave vector with modulus $k = 2\pi/\lambda$, where λ is the laser wavelength), V_c the cavity volume, and ϵ and V being the electric permittivity and the volume of the of silica sphere, respectively.
Assuming that the particle size is much smaller than the laser wavelength allows us to describe the particle as a simple dipole $P(\mathbf{r}') \approx \alpha_{ind}E(\mathbf{r})\delta(\mathbf{r}-\mathbf{r}')$, where $\mathbf{r}$ is the center of mass position of the nanosphere (here we are considering the motion along the cavity axis only, so that $\mathbf{r} = x\hat{\mathbf{x}}$) and α_{ind} its polarizability.
For a nanosphere oscillating near $x \approx 0$, and assuming a cavity field phase of $\phi = \pi/2$ (for maximizing the intensity field gradient at particle equilibrium position), the frequency shift becomes linear in x

$$\delta\omega_c^{lin} \approx -\frac{3V}{4V_c}\frac{(\epsilon-1)}{(\epsilon+2)}2kx\omega_{c0}, \tag{1.1.10}$$

provided the amplitude of nanosphere motion is smaller than the laser wavelength ($k\sqrt{\langle x^2\rangle} \ll 1$).
Eq. (1.1.10) tell us that the detuning $\Delta = \omega_L - \omega_c - \delta\omega_c^{lin}$ changes linearly with the particle's position on the cavity axis. Combining (1.1.10) with (1.1.5) we see that the cavity frequency shift caused by particle motion induces a change in the photon number and thus a change in the intracavity light intensity.

Next, we want to show the effect of the radiation pressure force of the cavity field on the particle motion. For this purpose, we expand the Hamiltonian of the cavity field in a Taylor series for a small displacement (compared to the laser wavelength) of the nanosphere motion x:

$$\begin{aligned}\hat{H}_{cav} = \hbar\omega_c\hat{a}^\dagger\hat{a} = \hbar(\omega_{c0}+\delta\omega_c)\hat{a}^\dagger\hat{a} = \hbar\omega_{c0}\hat{a}^\dagger\hat{a} + \hbar\frac{\mathrm{d}\omega_c}{\mathrm{d}x}\bigg|_{x=0} x\hat{a}^\dagger\hat{a} + ... \\ \approx \underbrace{\hbar\omega_{c0}\hat{a}^\dagger\hat{a}}_{\text{Bare cavity}} - \underbrace{2kx\hbar G\hat{a}^\dagger\hat{a}}_{\text{Interaction}},\end{aligned} \tag{1.1.11}$$

where $G = \frac{3V}{4V_c}\frac{(\epsilon-1)}{(\epsilon+2)}\omega_{c0}$. The nanosphere feel thus a radiation pressure mean force coming from the interaction part of Eq. (1.1.11) ($\hat{H}_{int} = -2kx\hbar G\hat{a}^\dagger\hat{a}$)

$$F_{rad} = -\frac{\mathrm{d}\hat{H}_{int}}{\mathrm{d}x} = 2k\hbar G\hat{a}^\dagger\hat{a} \tag{1.1.12}$$

that has to be integrated in its equation of motion.

To summarize, the trapped particle oscillations shift the cavity resonance frequency, modifying the intracavity field as described by Eq. (1.1.2). Afterwards, the light field acts back on particle motion via radiation pressure force (1.1.12), so that the particle motion is fed back on itself with a phase delay. This process is known in the literature as dynamical back-action [15], and it is the basis of every experimental optomechanical realization [11].

Optomechanics equations of motion

The evolution of the composite system cavity+nanosphere is obtained by solving the coupled equations of motion for the complex cavity amplitude a (1.1.2) and the particle position x (1.1.6). Here we consider a semiclassical regime, following [16]:

$$m\ddot{x} = -m\Gamma_m\dot{x} - m\omega_m^2 x + 2k\hbar G\hat{a}^\dagger\hat{a} + F_{ext} \tag{1.1.13}$$

$$\dot{\hat{a}} = -\frac{\kappa}{2}\hat{a} + i(\Delta + 2kGx)\hat{a}. \tag{1.1.14}$$

The solution of this system is obtained by first linearizing both the cavity amplitude around a classical steady state solution (see Eq. (1.1.4)) $\hat{a} = \bar{\alpha} + \delta a$, and the nanosphere center of mass position $x = \bar{x} + \delta x$, obtaining

$$m\delta\ddot{x} = -m\Gamma_m\delta\dot{x} - m\omega_m^2\delta x + 2k\hbar G\big(\bar{\alpha}^*\delta a + \bar{\alpha}\delta a^*\big) + F_{ext} \tag{1.1.15}$$

$$\delta\dot{a} = (i\Delta - \frac{\kappa}{2})\delta a + i2kG\delta x\bar{\alpha}. \tag{1.1.16}$$

Then we compute their Fourier transforms

$$-m\omega^2\delta x(\omega) = -i\omega m\Gamma_m\delta x(\omega) - m\omega_m^2\delta x(\omega) + 2k\hbar G\big(\bar{\alpha}^*\delta a(\omega) + \bar{\alpha}\delta a^*(\omega)\big) + F_{ext}(\omega) \tag{1.1.17}$$

$$i\omega\delta a(\omega) = \big(i\bar{\Delta} - \frac{\kappa}{2}\big)\delta a(\omega) + i2kG\bar{\alpha}\delta x(\omega), \tag{1.1.18}$$

where $\bar{\Delta} = \Delta + 2kG\bar{x}$ is the new effective detuning caused by the displaced center of the nanosphere oscillation due to the constant radiation pressure force.

Finally, by substituting the expression for $\delta a(\omega)$ as given by (1.1.18) in (1.1.17) we obtain a modified susceptibility χ

$$\chi(\omega) = \frac{1}{m(\omega_m^2 - \omega^2 - i\omega\Gamma_m) + S(\omega)}, \tag{1.1.19}$$

where

$$S(\omega) = -2im\omega_m g^2\left(\frac{1}{-i\bar{\Delta} - i\omega + \kappa/2} - \frac{1}{i\bar{\Delta} + i\omega + \kappa/2}\right) \tag{1.1.20}$$

and we have also introduced the so-called optomechanical coupling strength $g = 2\sqrt{\frac{\hbar}{2m\omega_m}}kG|\bar{\alpha}|$.
By separating the imaginary and real part of the susceptibility, one can see that the optomechanical coupling manifests itself by effectively changing both the spring constant and the mechanical dissipation rate of the nanosphere center-of-mass motion by the amount Γ_{opt} and $\delta\omega_m$, respectively, which, when evaluated at $\omega = \omega_m$, are given by

$$\delta\omega_m = \frac{1}{m}\mathrm{Re}[S(\omega_m)] = 2\omega_m g^2\left(\frac{\omega_m + \bar{\Delta}}{(\omega_m + \bar{\Delta})^2 + (\kappa/2)^2} - \frac{\omega_m - \bar{\Delta}}{(\omega_m - \bar{\Delta})^2 + (\kappa/2)^2}\right) \tag{1.1.21}$$

and

$$\Gamma_{opt} = -\frac{1}{m\omega_m}\mathrm{Im}[S(\omega_m)] = g^2\kappa\left(\frac{1}{(\omega_m + \bar{\Delta})^2 + (\kappa/2)^2} - \frac{1}{(\omega_m - \bar{\Delta})^2 + (\kappa/2)^2}\right). \tag{1.1.22}$$

Eq. (1.1.22) shows that in the red-detuned regime, when $\bar{\Delta} < 0$, the dissipation of the nanosphere's motion $\Gamma_{tot} = \Gamma_m + \Gamma_{opt}$ increases, leading to cooling of the mechanical motion. Conversely, in the blue-detuned regime, when $\bar{\Delta} < 0$, the dissipation decreases, with a subsequent increase in the particle fluctuations.

The optomechanically induced frequency shift (1.1.21) and the optomechanical damping (1.1.22) have both

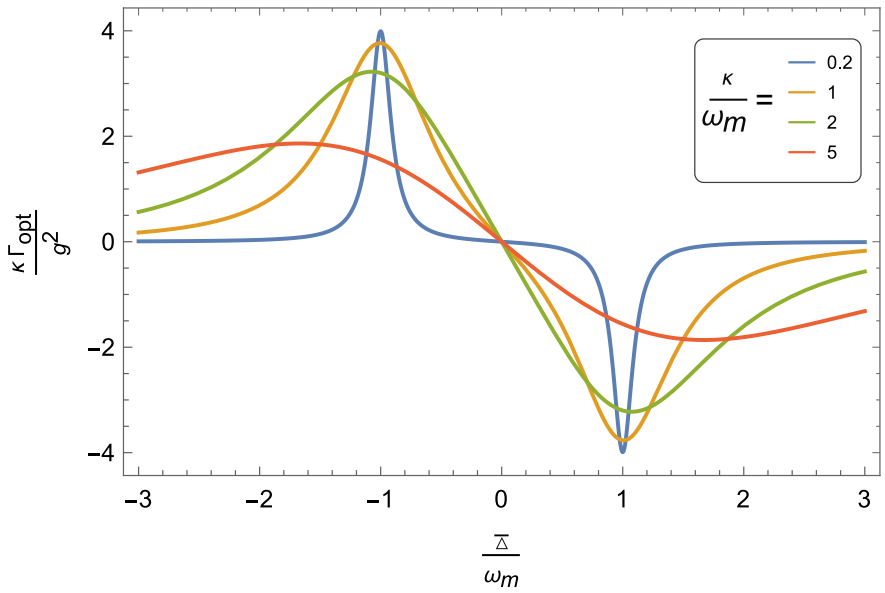

Figure 1.2: Optomechanical damping rate Γ_{opt} as function of the detuning $\bar{\Delta}$ for different cavity decay rate κ.

been experimentally demonstrated in the framework of levitated nanosphere experiments [17, 18].

In comparison with the coupling to the thermal environment at 300 K (room temperature) via Γ_m, this optical dissipation couples to a photon thermal bath that is effectively at $T_{eff} = 0$. Thus, in this case, the dissipation does not add thermal fluctuations to the system as it would in a conventional thermal bath.
This allows us to define an effective steady state temperature

$$T = T_{bath}\frac{\Gamma_m}{\Gamma_m + \Gamma_{opt}} \tag{1.1.23}$$

that can be related to a mean phonon number through the expression

$$\langle n \rangle = \frac{k_B T}{\hbar \omega_m} \tag{1.1.24}$$

where k_B is the Boltzmann constant.
No research group, however, has yet been able to demonstrate cooling rates high enough to enter into the quantum regime, i.e., reaching a phonon occupation number $\langle n \rangle < 1$ [19].

Within our semiclassical derivation, one needs to work in the resolved sideband-regime $\omega_m \gg \kappa$ to reach the minimum temperature, which is achieved for a red detuning of $\bar{\Delta} = -\omega_m$, and yields

$$\Gamma_{opt} \approx 4\frac{g^2}{\kappa}. \tag{1.1.25}$$

The full quantum treatment provides similar quantitative results [11], as the linearization of the cavity field carries away all the non-linear interactions that would result in the generation of non-classical states.

1.2 Cavity optomechanics assisted by a qubit

Novel cooling schemes and enhanced optomechanical coupling can arise as soon as a nonlinear element such a two-level quantum system (qubit) is introduced in an optomechanical setup. Pirkkalainen et al. [20] have coupled a Josephson junction qubit to their optomechanical system based on a microwave-regime superconducting cavity, showing an increase by six order of magnitude in the radiation pressure interaction, and nonlinear phenomena at single-photon energies scales. Moreover, a theoretical proposal suggests that non-classical states of the mechanical oscillator can be prepared by engineering the environment of a tripartite system consisting of the cavity, the mechanical oscillator and the qubit [7].
In our levitated optomechanics experiment, an interacting two level system can be engineered by coupling a single ion to the same cavity mode as the nanosphere [21], exploiting the well established protocols used in the field of cavity quantum electrodynamics [22].

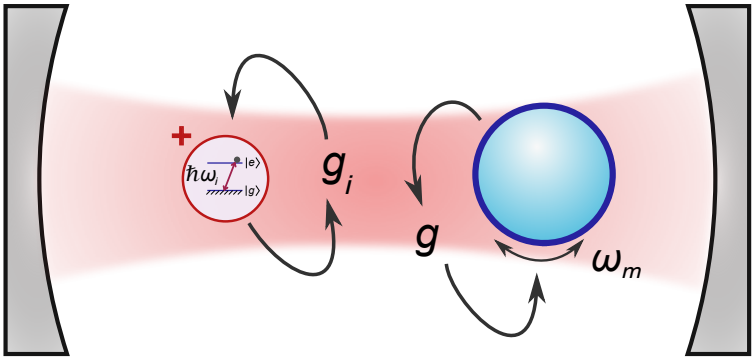

Figure 1.3: Schematic representation of the system composed by an optical cavity coupled to both a qubit and a nanosphere with coupling strength g_i and g, respectively. The nanosphere is oscillating within its trap at the frequency ω_m, and the internal energy states separation of the qubit is $\hbar\omega_i$.

The planned system is depicted in Fig. (1.3). A single calcium ion is harmonically trapped in a Paul trap and coupled to the cavity field via the Jaynes–Cummings Hamiltonian [23], so that the total Hamiltonian is given by

$$\hat{H}_{tot} = \hat{H}_{nano} + \hat{H}_{ion} + \hat{H}_{cavity} + \hat{H}_{int}^{nano-cav} + \hat{H}_{int}^{ion-cav} + \hat{H}_{drive}. \tag{1.2.1}$$

The first term on the right-hand side represents the Hamiltonian of the bare mechanical oscillations of the nanosphere $\hat{H}_{nano} = \hbar\omega_m \hat{b}^\dagger \hat{b}$ with $\hat{b}$ and $\hat{b}^\dagger$ being the annihilation and creation operators of a phonon. The second term is $\hat{H}_{ion} = \hbar\omega_i \hat{\sigma}_z$, where $\hbar\omega_i$ is the energy separation between the excited state $|e\rangle$ and ground state $|g\rangle$ of the qubit and $\hat{\sigma}_z$ is the z Pauli matrix. The third term $\hat{H}_{cavity} = \hbar\omega_{c0}\hat{a}^\dagger\hat{a}$ is the bare cavity Hamiltonian. The optomechanical interaction Hamiltonian is derived in Eq. (1.1.11) as $\hat{H}_{int}^{nano-cav} = -2k\hbar G x_{ZPM}(\hat{b}+\hat{b}^\dagger)\hat{a}^\dagger\hat{a}$, where we have replaced x with its quantum mechanical operator $\hat{x} = x_{ZPM}(\hat{b}+\hat{b}^\dagger)$ with $x_{ZPM} = \sqrt{\hbar/2m\omega_m}$ being the mechanical zero-point motion of the nanosphere. The interaction Hamiltonian between the ion and the cavity field is

$$\hat{H}_{int}^{ion-cav} = \hbar g_i(\hat{a}\hat{\sigma}^+ + \hat{a}^\dagger\hat{\sigma}^-), \tag{1.2.2}$$

where $\hat{\sigma}^- = |g\rangle\langle e|$ and $\hat{\sigma}^+ = |e\rangle\langle g|$ are the respectively lowering and raising operators that connect the excited and ground states of the qubit, and g_i is the atom-cavity coupling strength [24]. Finally, the laser drive is taken into account by the term $\hat{H}_{drvive} = \xi(\hat{a}e^{i\omega_L t} + \hat{a}^\dagger e^{-i\omega_L t})$, where ξ is the strength of the driving field oscillating at the frequency ω_L.

Pflanzer et al. [7] have suggested that in the regime where $g_i/|\Delta - \delta| \ll 1$, $g/|\Delta - \omega_m| \ll 1$, the cavity mediates an effective interaction between nanosphere and ion [7]. Here $\delta = \omega_i - \omega_L$ is the detuning of the qubit from the laser frequency. In this regime, the cavity degree of freedom can be eliminated from the

description of the system (see [7] for the derivation), leading to the new effective Hamiltonian

$$\hat{H}_{eff} = \frac{\hbar\tilde{\delta}}{2}\hat{\sigma}_z + \hbar\tilde{\omega}_m\hat{b}^\dagger\hat{b} - \hbar g_{i-m}(\hat{\sigma}^+\hat{b} + \hat{\sigma}^-\hat{b}^\dagger), \tag{1.2.3}$$

where $\tilde{\delta} = \delta - 2g_i^2/(\Delta - \delta)$, $\tilde{\omega}_m = \omega_m - 2g^2/(\Delta - \omega_m)$, and the coupling rate between the nanosphere motion and the ion is $g_{i-m} = g_i g(2\Delta - \omega_m - \delta)/[(\Delta - \delta)(\Delta - \omega_m)]$.

Eq. (1.2.3) is in the form of a Jaynes-Cummings interaction Hamiltonian (1.2.2), with the cavity light field replaced by the amplitude of quantum oscillation of the nanosphere. In this regime, it thus appears possible to prepare non-classical states like, for example, arbitrary Fock states [25].

Discussion

In this chapter, a basic introduction to the optomechanical coupling of an oscillating dielectric nanosphere with a cavity field have been presented. Then we have derived the equations of motion for both the mechanical oscillator and the cavity field. In the last part, we have written down the effective Hamiltonian that describes the system when a qubit is incorporated into the system, and how this can be engineered to prepare non-classical states of motion of the nanoparticle center of mass.

This thesis, however, will be focused on studying the trapping environment necessary to harmonically confine the nanosphere and the single ion.

Since it carries electrical charges, the ion can be confined by an electrodynamic Paul trap. The next chapter will provide therefore a basic introduction to Paul trap theory, along with a novel proposal to use the trap for trapping both species together, the nanosphere and the ion.

Chapter 2

Paul trap theory

The main requirements of building a levitated cavity optomechanics system are to implement a levitated mechanical oscillator and to isolate it from the various sources of decoherence due to the surrounding environment. The state of the art in current experiments is to use an optical tweezers or a Paul traps in order to provide a trapping field for confine the nanoparticle inside a vacuum chamber. Since the planned experiment in Innsbruck require the presence of a single calcium ion to assist the optomechanical coupling (see Sec. 1.2), it is convenient for us to use a Paul trap for simultaneously confine both the nanosphere and the ion.

Electrodynamic Paul traps [26] are based on the ponderomotive mean force felt by a charged particle in a quadrupolar time-oscillating electric potential. The strength of the trapping potential is weighted by the charge-to-mass ratio of the trapped particle. As a result, a good trap (that is, a deep trap) for a single calcium ion could be at the same time a very shallow well for a massive object like a 100 nm diameter silica nanosphere, which has a mass of $M_{nano} \sim 10^7 M_{^{40}\mathrm{Ca}^+}$. Charging methods for levitating dielectric spheres, that includes ion or electron bombardment [27], electrospray ionization (see Chap. 3.2.1) and corona discharge [27], can provide a typical charge of $Q_{nano} \sim 100$ [28], that is not enough to solve the high mismatch of the charge-to-mass ratios with the single calcium ion, that is assumed to have a single charge. Therefore, the difference between the charge-to-mass ratios prevents stable trapping of both particles. To circumvent this problem, a recent theoretical proposal [8] (endorsed by preliminary experimental results [29] that show the effects of the second frequency field on the stability of a trapped calcium ion) suggests that using a Paul trap driven by two frequency sources can effectively trap two ion species even if their charge-to-mass ratios are very different.

In the first part of this chapter, the basic principle of ion trapping in a Paul trap will be introduced.

Afterwards, the two-frequency approach will be studied with more detail in order to give a theoretical estimation regarding possible sets of parameters, both for the goal of trapping a single calcium ion together with a silica nanosphere and for a first experimental test within the framework of a rescaled system for a preliminary assessment.
Finally, the operation of the Paul trap as a charge-to-mass spectrometer will be briefly explained.

2.1 The linear Paul trap theory

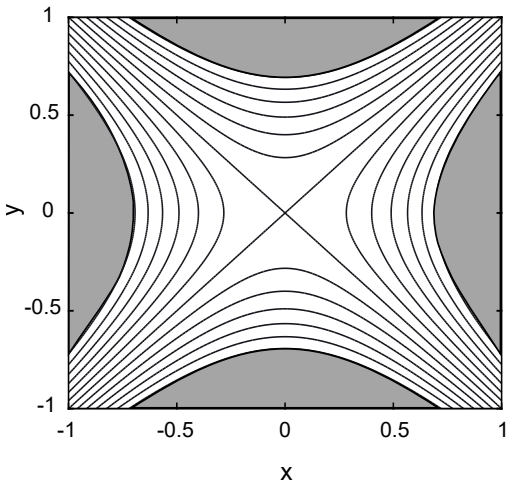

Figure 2.1: Equipotential lines of a two-dimensional quadrupole electric potential. When the voltage of two diametrically opposed electrodes oscillates sinusoidally in time, the resulting ponderomotive force can trap ions, regardless of the sign of their charge.

A Paul trap consists of an arrangement of electrodes combined to form a non-vanishing quadrupole moment (see Fig. (2.1)) of the electric potential φ. The ideal situation can be achieved for any geometry that satisfies the Laplace equation

$$\nabla^2\varphi(x,y,z) = 0 \tag{2.1.1}$$

with

$$\varphi(x,y,z) = U\frac{1}{2}(\alpha x^2 + \beta y^2 + \gamma z^2), \tag{2.1.2}$$

where x, y and z are the three orthogonal spatial coordinates, U is the applied voltage and α, β and γ are real geometrical constants characterizing profile and relative distances of the electrodes.
Since Eq. (2.1.1) imposes that

$$\alpha + \beta + \gamma = 0, \tag{2.1.3}$$

at least one of the coefficients has to be negative. This means that an applied electrostatic potential can not provide a restoring force in every spatial direction[1]. A dynamical equilibrium is reached, though, if a

[1]This fact is also known as Earnshaw's theorem, after the British mathematician Samuel Earnshaw who first prove it in 1842.

sinusoidally oscillating part is added to the static potential [26]:

$$\varphi(x,y,z,t) = U\frac{1}{2}(\alpha x^2 + \beta y^2 + \gamma z^2) + U_{RF}\cos(\Omega t)\frac{1}{2}(\alpha' x^2 + \beta' y^2 + \gamma' z^2), \tag{2.1.4}$$

where U_{RF} is the amplitude of the AC field oscillating at the rf frequency Ω, and α', β' and γ' are geometrical factors that satisfy the same relation of Eq. (2.1.3), namely,

$$\alpha' + \beta' + \gamma' = 0. \tag{2.1.5}$$

We will see below how a particular choice of U, U_{RF} and Ω will lead to an effective restoring force in all three spatial dimensions.

For a linear trap, the geometrical coefficients are chosen to be [30]

$$\begin{aligned} -(\alpha+\beta) = -2\alpha = \gamma = \frac{1}{z_0^2} \\ \alpha' = -\beta' = \frac{1}{r_0^2}, \end{aligned} \tag{2.1.6}$$

where $2r_0$ and $2z_0$ are the distances between the radial and the axial electrodes (the latter are usually referred as endcap electrodes), respectively (see Fig. 2.2 (b)).

In this fashion, dynamical confinement is used to trap on the xy-plane, and a static field along $\hat{z}$ provides axial trapping for charged particles.

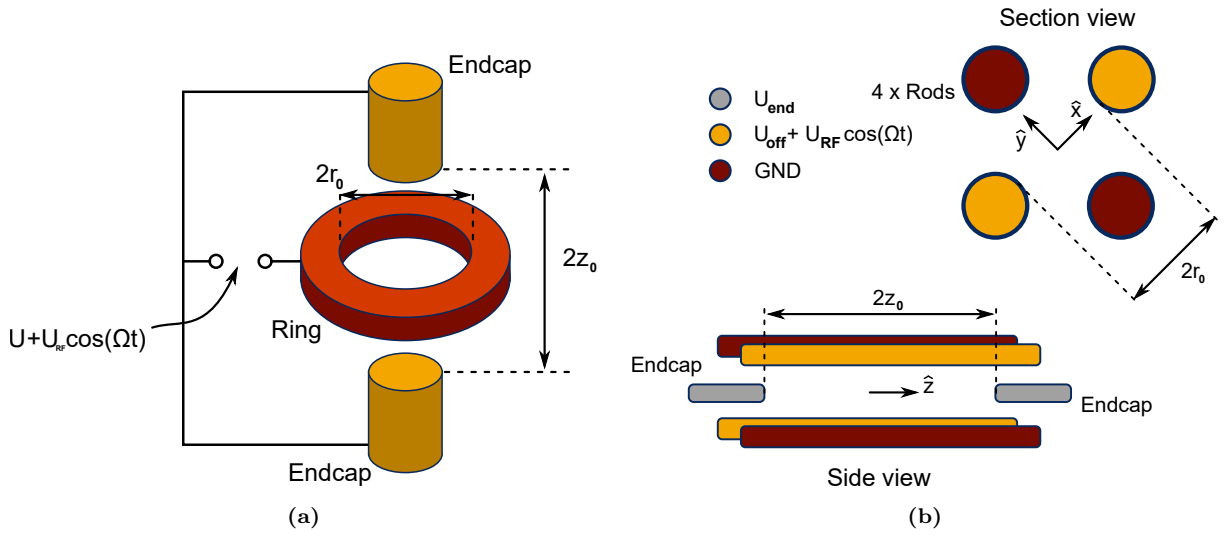

Figure 2.2: Typical realizations of a Paul trap: (a) ring Paul trap. The ideal geometrical coefficients for this configuration are $\alpha = \beta = \gamma = 0$ and $\alpha' + \beta' = -\gamma'$, which give a full three-dimensional symmetric potential useful for trapping a single particles. (b) Linear trap. The ideal geometrical coefficients for this configuration are given in Eq. (2.1.6). By substituting the hyperbolic profile of an ideal trap with electrodes with a circular cross section, the effective volume of the trap is reduced (see simulations in Fig. 3.3). In the four cylinders linear trap, two diametrically opposite rods are driven with an oscillating voltage $U_{RF}\cos(\Omega t)$ plus a DC offset U_{off}, while the other two are grounded. The axial electrodes (endcaps) are held at the static voltage U_end. To note that in the linear trap geometry the zero of the RF field is along the whole $\hat{z}$ axis while in the ring trap is only the single point located at the center of the trap.

Equation of motion

The equation of motion along the $\hat{x}$ axis for a particle of mass m and electric charge Q subject to the potential (2.1.4) with the ansatz (2.1.6) is

$$m\ddot{x} = -Q\frac{\partial \varphi}{\partial x} = -Q\Big(- \frac{U_{end}}{z_0^2} - \frac{U_{off}}{r_0^2} - \frac{U_{RF}}{r_0^2}\cos(\Omega t)\Big)x, \tag{2.1.7}$$

where U_{end} is the static field produced by the endcap axial electrodes, and U_{off} accounts for a possible DC offset of the oscillating potential. For the moment, we have also neglected every source of damping. Following [31], Eq. (2.1.7) can be recast in the form of a Mathieu equation [32]:

$$\frac{\mathrm{d}^2 x}{\mathrm{d}t_1^2} + (a_x - 2q_x\cos(2t_1))x = 0, \tag{2.1.8}$$

where we have used the following substitutions:

$$a_x = -\frac{4Q}{m\Omega^2}\Big(\kappa\frac{U_{end}}{z_0^2} + \frac{U_{off}}{r_0^2}\Big), \tag{2.1.9}$$

$$q_x = \frac{2QU_{RF}}{mr_0^2\Omega^2}, \tag{2.1.10}$$

$$t_1 = \frac{\Omega t}{2}. \tag{2.1.11}$$

Eq. (2.1.8) is indeed an approximation valid near the axis of a real linear Paul trap. Moreover, the non-ideal shape of the axial electrodes is taken into account with the dimensionless factor κ, which assumes its maximum value $\kappa = 1$ for hyperbolic endcap electrodes.

The equations of motion on the $\hat{y}$ and $\hat{z}$ axes are of the same form as Eq. (2.1.8) with the parameters

$$y\big) \quad a_y = -\frac{4Q}{m\Omega^2}\Big(\kappa\frac{U_{end}}{z_0^2} - \frac{U_{off}}{r_0^2}\Big), \quad q_y = -q_x \tag{2.1.12}$$

$$z\big) \quad a_z = \kappa\frac{8QU_{end}}{mz_0^2\Omega^2}, \quad q_z = 0. \tag{2.1.13}$$

The Mathieu equation of motion (2.1.8) is an ordinary differential equation (ODE) with periodic coefficients. Floquet theory [32] can be used to express the solution of Eq. (2.1.8) in the form of an infinite series

$$x(t_1) = Ae^{\pm i\beta_x t_1}\sum_{r=-\infty}^{\infty} C_{2r}e^{2irt_1} + Be^{\mp i\beta_x t_1}\sum_{r=-\infty}^{\infty} C_{2r}e^{-2irt_1}, \tag{2.1.14}$$

where A and B are constants to be determined by the initial conditions of a particular problem, and β_x is a parameter that depends on the coefficients a_x and q_x.

The value of β_x governs the behavior of the solutions: the trap is stable (i.e., the motion is spatially bounded) if β_x is real and not an integer; the trap is unstable instead if the value of β_x is purely imaginary. The case for which β_x is an integer represents the boundary between stable and unstable motion.

By substituting Eq. (2.1.14) into the equation of motion (2.1.8), we obtain a recursive implicit equation for β_x:

$$C_{2r} + D_{2r}\big[C_{2r+2} + C_{2r-2}\big] = 0, \tag{2.1.15}$$

with $D_{2r} = [q_x/(2r+\beta_x)^2 - a_x]$. Therefore, the stability boundaries can be numerically calculated as the integer isoline values of β_x within the domain of the a_xq_x-plane.

An analogous treatment can be done for the y component of the equation of motion, with the parameters a_y, q_y and β_y.

Fig. (2.3) shows the stability diagram of motion along x obtained with the code included in Appendix A. In order to have stable confined motion along all three spatial axes of the trap, all members of the set of parameters a_i and q_i with $i = \{x, y, z\}$ must lie within their respective stability zones. For a linear trap, this

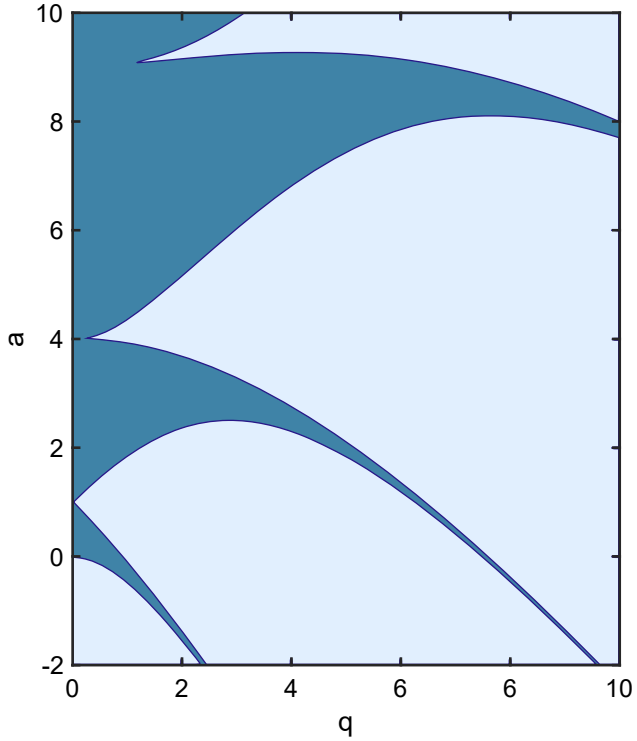

Figure 2.3: Stability diagram of the Mathieu equation, corresponding to the normalized dimensionless equation of motion along the $\hat{x}$ axis for a charged particle in a linear Paul trap (see text). At fixed operating trap's frequency and without any applied DC offset on the RF electrodes ($U_{off} = 0$), q is proportional to the voltage of the RF field U_{RF} while a is proportional to the endcap voltage U_{end}. Stable (unstable) solution are obtained for a and q lying in the light (dark) area.

means that the system has to be in the intersection of the stable zone of just the x and y branches, since the axial electric field is always confining ($a_z > 0$, $q_z = 0$).

The radially defocusing DC field induced by U_{end} is typically less strong than the radial confinement, for two reasons: first, the axial endcap electrode separation $2z_0$ is always larger than the radial distance $2r_0$ between the rods; second, the non-ideal axial quadrupolar field, quantified by the coefficient $\kappa < 1$, reduces the effect of the endcaps on the radial confinement. For these reasons, we can assume $a_x \approx -a_y$, meaning that the stability diagrams of the x and y motion are mirror images of each other, as depicted in Fig. (2.4) (B).

The region delimited by the intersection of the first stable branches of x and y (i.e., the common area between the curves $\beta_x = \{0, 1\}$ and $\beta_y = \{0, 1\}$) is typically referred to as the first stability zone. As comparison, the second stability zone (i.e., the common area between the curves $\beta_x = \{0, 1\}$ and $\beta_y = \{1, 2\}$) is shown

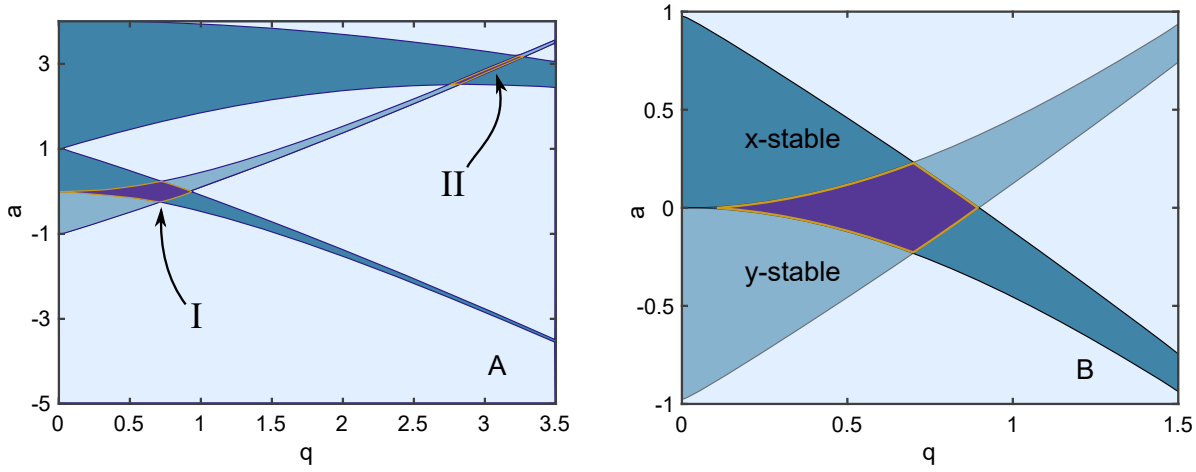

Figure 2.4: (**A**): first and second stability regions (purple) of the linear Paul trap. (**B**): zoom of the first stability region of the linear Paul trap. The maximum stable q value is $q_{max} \sim 0.9$.

in Fig. (2.4) (A). Due to the higher accessible parameters (namely, voltages and frequencies) suitable for stable trapping, the first stability zone is preferred. Moreover, in the limit $\beta_{x,y} \ll 1$, the motion inside the trap becomes nearly harmonic, with frequencies $\omega_{x,y} = \beta_{x,y}\Omega/2$ along x and y respectively. This can be demonstrated by the so called pseudopotential approximation.

The pseudopotential approximation

Since in the typical experimental realization of a linear Paul trap, the a_x parameter is always kept close to zero, in the following calculations we will neglect it. This will also make the calculations easier.
With this in mind, the equation of motion (2.1.7) can been seen as a harmonic oscillator with a time modulated frequency $\omega(t)$ such that

$$\omega(t)^2 = \frac{QU_{RF}}{mr_0^2}\cos(\Omega t) = \frac{q_x\Omega^2}{2}\cos\Omega t \tag{2.1.16}$$

The system has thus two characteristic frequencies: Ω, the one at which the field changes polarity, and the static part of $\omega(t)$. The pseudo-potential approximation is based on a large separation between these two frequencies, namely $\Omega \gg \sqrt{\frac{q_x}{2}}\Omega$, i.e., $q_x \ll 1$. The two very different time scales suggest a subdivision of the motion into a smooth, slow time varying path plus a fast oscillating amplitude [33]

$$x(t) = X(t) + \xi(X,t). \tag{2.1.17}$$

Here X represents the mean displacement of the particle in a period $T = 2\pi/\Omega$ of the fast oscillation, meaning that for the fast varying term, $\langle\xi\rangle_T = \frac{1}{T}\int_0^T \xi(t)dt = 0$.
Another assumption that will be verified in the end of the calculation is that

$$\xi \ll X. \tag{2.1.18}$$

For these reasons X is called the secular motion and ξ the micromotion.
Following [34] we insert (2.1.17) into Eq. (2.1.7) (always neglecting static terms involving a_x):

$$m(\ddot{X} + \ddot{\xi}) = -\frac{q_x\Omega^2}{2}\cos(\Omega t)(X + \xi). \tag{2.1.19}$$

This equation contains both smooth and fast oscillating parts that have to be independently equal.
The fast term is

$$m\ddot{\xi} = -\frac{q_x\Omega^2}{2}\cos(\Omega t)X, \tag{2.1.20}$$

where we have neglected the smallest term proportional to ξ because $\ddot{\xi} \sim \Omega^2\xi$ is a large quantity.
From Eq. (2.1.20) we obtain for the amplitude of micromotion

$$\xi = \frac{q_x X}{2}\cos(\Omega t). \tag{2.1.21}$$

Putting this value for the amplitude back inside Eq. (2.1.19) and averaging over one period of the fast oscillation, we get the equation for the slow secular motion

$$m\ddot{X} = -\frac{m}{2}\Big(\frac{q_x\Omega}{2}\Big)^2 X \tag{2.1.22}$$

which corresponds to a harmonic oscillator with the secular frequency

$$\omega_x = \frac{q_x\Omega}{2\sqrt{2}}. \tag{2.1.23}$$

Thus the complete equation of motion now can be written as

$$x(t) = X + \xi = A\cos(\omega_x t)\big(1 + \frac{q_x}{2}\cos(\Omega t)\big) \tag{2.1.24}$$

where the fast micromotion oscillations at the driving frequency Ω are over imposed on a slow secular harmonic oscillation at frequency ω_x, with an amplitude A which depends on the initial conditions.
Since we work with $q_x \ll 1$, the amplitude of micromotion is low, and this is consistent with the initial assumption (2.1.18). Eq. (2.1.22) could be rewritten in terms of an effective potential

$$m\ddot{X} = -\frac{\partial\varphi_{eff}}{\partial X}, \tag{2.1.25}$$

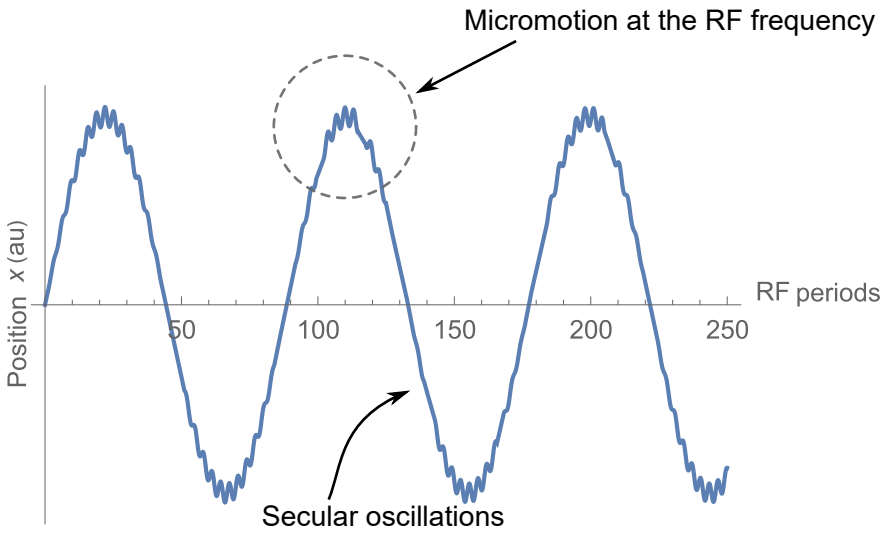

Figure 2.5: Secular motion and micromotion inside a Paul trap obtained thanks to the pseudopotential approximation valid in the $q \ll 1$ regime.

with

$$\varphi_{eff} = \frac{1}{2} m\omega_x^2 X^2. \tag{2.1.26}$$

Finally, we can calculate the pseudopotential depth $\overline{D}_x$ of our trap, within the approximations made so far, as

$$\overline{D}_x = \int_{X=0}^{X=r_0} \frac{\partial \varphi_{eff}}{\partial X} dX = \frac{m\Omega^2 r_0^2}{16} q_x^2 = \frac{QU_{RF}^2}{4mr_0^2\Omega^2} \tag{2.1.27}$$

An analogous treatment can be done with the y component of the equation of motion. Since in the linear trap $q_x = -q_y$, the oscillatory motion along $\hat{y}$ occurs at the same frequency $\omega_x = \omega_y$, and thus the effective potential is radially symmetric.

For the axial motion along $\hat{z}$, the presence of a DC field alone implies

$$\ddot{z} = \kappa \frac{2QU_{end}}{mz_0^2} z, \tag{2.1.28}$$

that is, a harmonic oscillator with frequency $\omega_z = \sqrt{\frac{\kappa 2QU_{end}}{mz_0^2}}$.

Discussion

We have shown how a linear Paul trap can lead to a stable or unstable motion depending on the particular choice of the driving voltages and frequencies of the electrodes. We have also demonstrated that within the first stability zone and with $a \sim 0$, $q \ll 1$, the trapped charged particle oscillates harmonically along each spatial axis at the secular frequencies ω_x, ω_y and ω_z, with small residual motion called micromotion

superimposed at the drive frequency Ω.

In experiments with single or a few trapped atomic ions [35,36], typical parameters used to confine the ions harmonically are $a = 0$ and $q \lessapprox 0.4$. In this regime, one is sure not to induce parametric resonances [37] that could heat up the trapped ions.

2.1.1 The effect of damping on the stability diagrams

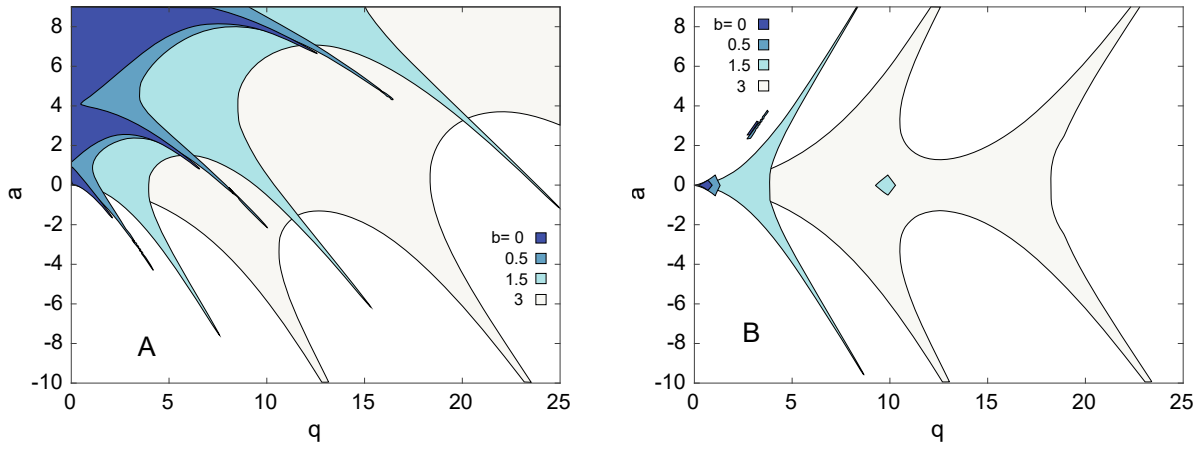

Figure 2.6: (**A**): stable solutions (colors) of the Mathieu equation in the presence of various damping strength. (**B**): first and second stability regions for stable trapping in the linear trap with different value of the damping strength. While the damping increases, the stable trapping zone get larger and shifted compared to the $b = 0$ case. Moreover, after the value $b = 1.5$ the second stability region become incorporated with the first one.

Mean viscous drag force resulting from collisions with background gas can be taken into account in the equation of motion of a trapped particle by means of a damping term. Moreover, a damping term can also effectively describe, for example, laser [38] and buffer gas cooling [39] of the ion, and feedback and cavity cooling of the center-of-mass motion of a silica nanosphere (cf. Chap (1.1)) [18,40,41].

Thus, it is worth rewriting the x component of the equation of motion (2.1.7) to include a viscous friction-like term proportional to the particle's velocity [42]:

$$m\ddot{x} = -\gamma\dot{x} + \Big(\frac{QU_{end}}{z_0^2} + \frac{QU_{off}}{r_0^2} + \frac{QU_{RF}}{r_0^2}\cos(\Omega t)\Big)x, \tag{2.1.29}$$

where γ is the coefficient describing a characteristic damping mechanism.

Even if $\gamma \neq 0$, Eq. (2.1.29) can be recast in the form of a Mathieu equation: we first perform the usual

substitution (2.1.9), obtaining

$$\frac{\mathrm{d}^2x}{\mathrm{d}t_1^2} + 2b\frac{\mathrm{d}x}{\mathrm{d}t_1} + (a_x - 2q_x\cos(2t_1))x = 0, \tag{2.1.30}$$

where we have set

$$b = \frac{\gamma}{m\Omega}. \tag{2.1.31}$$

Then, using the transformation $x = u\exp(-bt_1)$ we get

$$\frac{\mathrm{d}^2u}{\mathrm{d}t_1^2} + (a_x - b^2 - 2q_x\cos(2t))u = 0, \tag{2.1.32}$$

that is, a Mathieu equation with the parameter a_x replaced by $a_x - b^2$.
The same formalism of Sec. (2.1) can thus be applied, and the new stability diagrams can be calculated with the code presented in Appendix A.
Fig. (2.6) shows what happens for different increasing values of b. As one would expect, higher damping means larger stable regions. At the same time, however, stable zones are shifted in position [43], potentially giving unstable character to an otherwise stable point of operation with $b = 0$.

2.2 Paul trap driven by two frequencies

Paul traps have been typically used to investigate the properties of trapped objects such as a cloud of ions. For a system like an ion cloud with many degrees of freedom, an additional quadrupole field with lower amplitude than the primary one can be scanned while fluorescence of the ions is registered, leading to the appearance of various mechanical resonances. These resonances are mostly due to parametric excitations of the secular frequencies, higher-order modes of oscillation and nonlinearities of the trap potential. Thus, in these kinds of measurements, the second oscillating field is used to probe the system.

To understand the effect of this second field, we rewrite Eq. (2.1.29) taking into account a second driving with a different frequency and amplitude but with the same field geometry.
The equation of motion is now given by:

$$m\ddot{x} = -\gamma\dot{x} + \Big(\frac{QU_{end}}{z_0^2} + \frac{QU_{off}}{z_0^2} + \frac{QU_1}{r_0^2}\cos(\Omega_1 t) + \frac{QU_2}{r_0^2}\cos(\Omega_2 t)\Big)x, \tag{2.2.1}$$

where γ is the damping constant, m and Q are the mass and the charge of the trapped particle and U_i, Ω_i for $i = \{1, 2\}$ are the amplitude and the frequency of the first and the second oscillating potential, respectively. In order to simplify the calculations, we consider the second frequency Ω_2 to be a harmonic of the first one, so that $\Omega_2 = n\Omega_1$ with n an integer. For this reason, Ω_1 and Ω_2 will be called the slow frequency and the

fast frequency, respectively.

With the same transformation used in Eq. (2.1.9), we can recast the above equation of motion (2.2.1) as

$$\frac{\mathrm{d}^2x}{\mathrm{d}t_1^2} + 2b_1\frac{\mathrm{d}x}{\mathrm{d}t_1} + (a_x - 2q_x\cos(2t_1) - 2p_x\cos(2nt_1))x = 0, \tag{2.2.2}$$

where we have additionally used

$$p_x = \frac{2QU_2}{mr_0^2\Omega_1^2}, \tag{2.2.3}$$

$$\Omega_2 = n\Omega_1, \tag{2.2.4}$$

and where the index in b_1 emphasize that we have rescaled the time with respect to the slow frequency such that $b_1 = \gamma/(m\Omega_1)$ (cf. Eq. (2.1.9)).

Eq. (2.2.2) is a second-order linear ordinary differential equation with periodic coefficients, generally known in the literature as the Hill equation [32], of which the Mathieu equation (2.1.8) is just one particular case involving a single frequency.

As was done for the Mathieu equation (cf. Chap. (2.1)), we use Floquet theory to find an analytic solution to Eq. (2.2.2) in terms of an infinite series expansion: by substituting the ansatz (2.1.14) in (2.2.2) we get a recursive relation for find the β_x parameter, namely

$$C_{2r} + D_{2r}\big[C_{2r+2} + C_{2r-2}\big] + F_{2r}\big[C_{2r+2n} + C_{2r-2n}\big] = 0, \tag{2.2.5}$$

where $D_{2r} = [q_x/(2r+\beta_x)^2 - a_x b_1^2]$ and $F_{2r} = [p_x/(2r+\beta_x)^2 - a_x + b_1^2]$.

Eq. (2.2.2) has bounded and unbounded solutions in time, just as its single-frequency counterpart does, and these solutions depend on the particular values assumed by its β_x parameter. The boundary between stable and unstable motion is represented (for a fixed value of damping) by the isosurfaces at integer values of β_x in the three-dimensional parameter space spanned by $\big(a_x, q_x, p_x\big)$.

A slice in the $a_x = 0$ plane (that is, when no DC offset is applied to the trap electrodes) for different values of the frequency ratio $n = \Omega_2/\Omega_1$ is depicted in Fig. (2.7). The β_x parameter was evaluated with the code found in Appendix (A). Fig. (2.7) shows how the fast frequency Ω_2 induces $n-1$ tongues of subharmonic resonances that cut the stability zone down to the $q = 0$ axis.

For high value of n, these instabilities become denser and narrower. However, the finite resolution of the numeric code acts as an effective damping [44], limiting the visibility of the resonances near the horizontal axis.

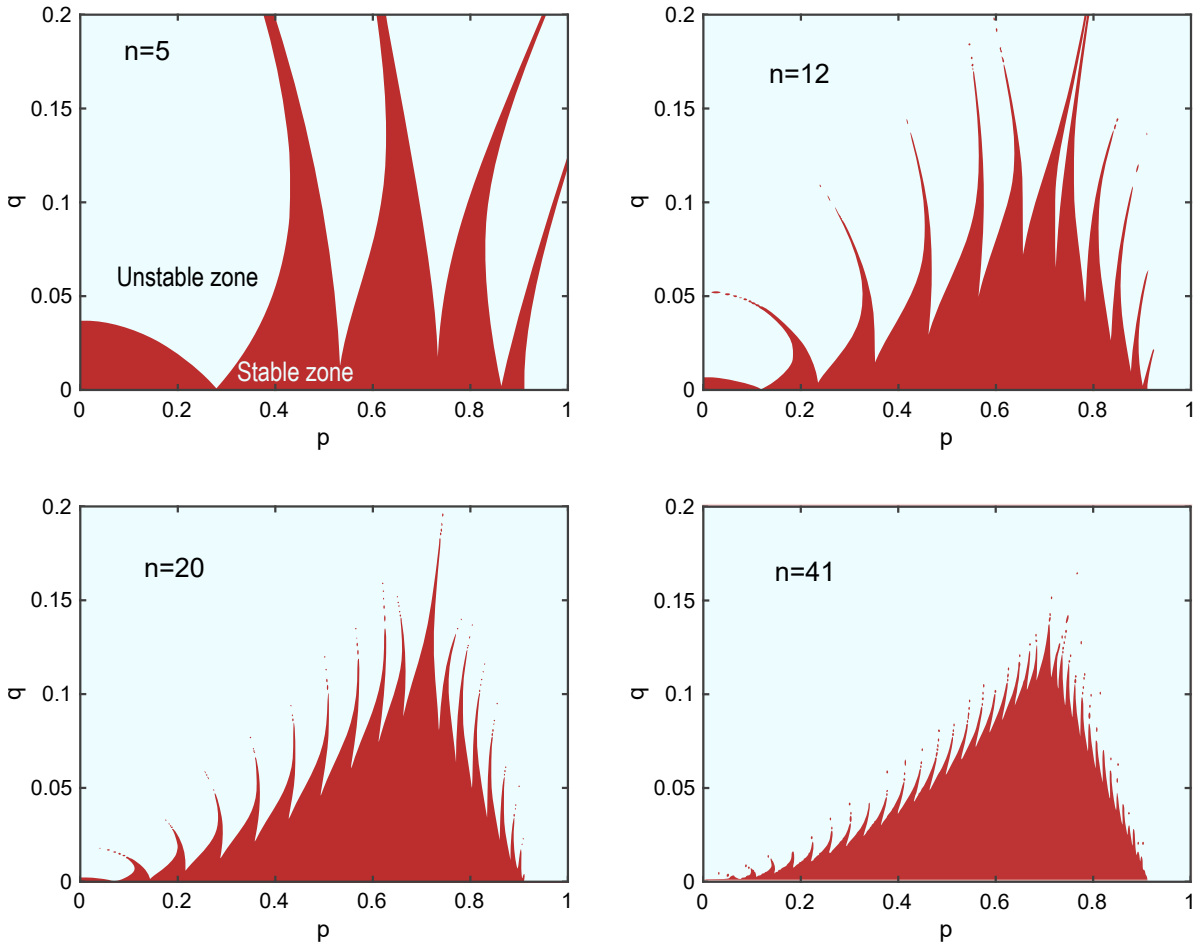

Figure 2.7: Stability diagrams for a two-frequency-driven Paul trap along the $a = 0$ plane. At a fixed operating frequencies, p is proportional to the strength of the field oscillating at the fast frequency Ω_2 while q is proportional to the strength of the field oscillating at the slow frequency $\Omega_1 = \Omega_2/n$. The slow field induced $n - 1$ parametric resonances which makes the trap unstable. The width of instability exponentially decay in reaching the $q = 0$ axis [44], making them difficult to resolve.

Discussion

The motional instabilities inside a Paul trap arising from parametric resonances induced by a second frequency have been studied in various experimental and theoretical works [45–47]. Recently, the two-frequency scheme was applied to the completely different task of stably trapping two ion species with a very large difference in their charge-to-mass ratios [8]. This theoretical proposal is gaining the attention of experimental groups that work with multiple ion species or larger charged objects in a Paul trap [29, 48]. The following section will provide a basic theoretical treatment for our case of interest: trapping a calcium ion together with a charged silica nanosphere.

2.2.1 Trapping two particles with one frequency

If one is interested in seeing some kind of local interaction between two different trapped species inside a Paul trap, it is desirable to put the the two objects as close together as possible. This situation arises for example in sympathetic cooling of atomic ions [49], or of even larger systems such as proteins [50].
Here, we are interested in trapping (A) a charged silica nanosphere and (B) a single $^{40}Ca^{+}$ ion. Their respective typical charge and mass values are shown in the following table.

Species	Mass (u)	Charge (e)
A) 100 nm silica sphere	6×10^8	100
B) $^{40}Ca^{+}$ single ion	40	1

We assume the silica sphere to have a diameter of 100 nm, with an electrical charge of[2] $100\,e$ [28]. Hence, we obtain

$$\frac{Q_B}{m_B} \approx 10^5 \frac{Q_A}{m_A}. \tag{2.2.6}$$

The main disadvantage of working with a single-frequency-driven Paul trap is that the resultant secular frequency (cf. Eq. (2.1.23)) felt by both particles is directly proportional to their charge-to-mass ratio:

$$\omega_i \propto \frac{Q_i}{m_i}, \tag{2.2.7}$$

where $i = \{A, B\}$. This leads to species-dependent spring constants $\kappa_i = m_i\omega_i^2 \propto Q_i^2/m_i$. In other words, the particle with the lowest Q/m value will experience a lower restoring force. Therefore, assuming thermal equilibrium at temperature T between the two species

$$k_B T = \kappa_i \langle x_i^2 \rangle, \tag{2.2.8}$$

where k_B is the Boltzmann constant, the nanosphere position fluctuations $\overline{x}_A = \sqrt{\langle x_A^2 \rangle}$ will be

$$\overline{x}_A = \overline{x}_B \sqrt{\frac{m_A}{m_B}} \frac{Q_B}{Q_A} \approx 10^3 \overline{x}_B. \tag{2.2.9}$$

Thus, a Paul trap driven with parameters (namely, voltage and frequency) optimized only for a single ion would lead to very large fluctuations in the nanosphere displacement, which would lead to the latter escaping the trap.

[2] As we will see later in the experimental part of the thesis (cf. Chap. (4.1.1)), this value of the charge for the nanosphere is larger than what we can achieve with the current loading techniques of our setup. In future work, it is planned to investigate adaptations of the loading technique as well as separate charging methods.

2.2.2 Trapping two particles with two frequencies

If we now drive the Paul trap with two frequencies at two different voltages optimized for individually trapping the nanosphere and the ion, the spring constant ratio no longer depends only on the charge-to-mass ratio, but also on the frequency and voltage used to obtain independent stable trapping of both species, namely

$$\frac{k_A}{k_B} \approx \frac{m_A\omega_A^2}{m_B\omega_B^2} \approx \left(\frac{U_A}{\Omega_2}\frac{\Omega_1}{U_B}\right)^2 \frac{Q_A^2/m_A}{Q_B^2/m_B}, \tag{2.2.10}$$

where we are supposing that the nanosphere is affected mainly by the field oscillating at Ω_2 with amplitude U_A, while the ion is confined by the Ω_1 frequency with amplitude U_B.
Thus, even if the charge-to-mass ratio of each species is fixed, it is possible to balance the spring constants $\kappa_A/\kappa_B \sim 1$ by tuning the two sets of frequencies and voltages.

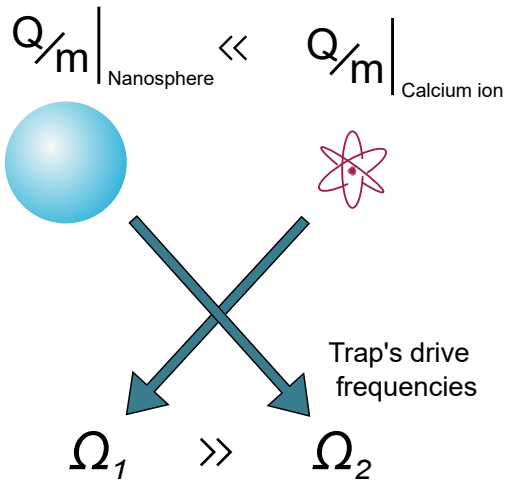

Figure 2.8: Due to the large charge-to-mass ratios separation between the calcium ion and a typical charged nanosphere, the fast frequency Ω_1 is used for trap the calcium ion while the slow frequency Ω_2 is used to trap the nanosphere.

Choosing the right voltage for the right frequency

We consider the fast driving frequency Ω_1 as a harmonic of the slow frequency Ω_2, namely

$$\Omega_1 = n\Omega_2 \tag{2.2.11}$$

with n an integer. The values of the two voltages and frequencies that make the spring constant ratio in Eq. (2.2.10) equal to one are not arbitrary. We impose on them two requirements:

- Each individual particle must be stably confined inside the trap;
- Parametric resonances induced by the slow trap frequency must be avoided.

First, in order to obtain a stable trapping inside the trap, we have to ensure that the q parameter for both species is

$$q_{A,B} \lesssim 0.4. \tag{2.2.12}$$

This requirement together with Eq. (2.2.10) fixes the drive frequency ratio, since

$$\frac{k_A}{k_B} = \frac{m_A\omega_A^2}{m_B\omega_B^2} = \frac{m_A\big(0.4\Omega_2\big)^2}{m_B\big(0.4\Omega_1\big)^2} = 1, \tag{2.2.13}$$

where we have used Eq. (2.1.23) to express the secular frequency ω as a function of q. Substituting the values for the masses of the species, and using a typical fast frequency for the calcium ion confinement of $\Omega_1 \sim 1\,\mathrm{MHz}$, we get $n \sim 10^3$.

Second, once we have chosen the driving frequency ratio n, the voltage ratio has to be chosen in order to avoid parametric instabilities, like those shown in Fig. (2.7).

With such a high frequency ratio ($n \sim 10^3$), it becomes very difficult to resolve all $n-1$ parametric resonances. However, we have seen in Chap. (2.1.1) how damping enlarges the stable region of operation of the trap. Thus, adding a damping mechanism such as the damping force arising from Doppler cooling cause the bottom tips of the instability tongues to lift up from the horizontal axis. Foot et al. [29] have shown how the threshold voltage of the slow field U_2 that can excite a parametric resonance is related to the dimensionless damping coefficient b_1 (cf. Eq. (2.1.9)) and to the fast field voltage U_1. They found that

$$U_2 = \rho \frac{Q_B}{m_B n^2 \Omega_2^2 r_0^2} U_1^2 (\pi b_1)^{1/m}, \tag{2.2.14}$$

where $\rho = 0.54$ is a constant, r_0 is the separation between the particle and the radial electrode in a linear trap (see Fig. (2.2) (b)), and the order number m is

$$m = \frac{2\omega_B}{\Omega_1} \approx \frac{n q_B}{\sqrt{2}} \approx 0.28 n, \tag{2.2.15}$$

where in the last equality we have used $q_B = 0.4$.

Thus, a suitable damping force on the ion, arising from a Doppler cooling mechanism or the pressure of the residual gas in the vacuum chamber, is sufficient to avoid instabilities that could limit the lifetime of the ion in the trap.

2.3 Paul trap as a mass spectrometer

Finally, we want to provide a basic introduction to the operation of a linear Paul trap as a charge-to-mass spectrometer, which will be a useful tool for understanding the nanosphere loading mechanism with the electrospray ionization technique (cf. Chap 3.2.1), the latter being known to generate a broad charge distribution among the launched particles (cf. Chap 4.1.1).

Let us consider in this regard a linear Paul trap, with frequency Ω and voltage U_{RF}. Then we know from Chap. (2.1) that confinement of charged particles occurs only within certain zones of the aq-plane, called stability regions.

Let us zoom into the first stability zone shown in Fig. (2.4) (B). Limiting our attention to the $a = 0$ axis, the highest reachable q-value is located at $q_{max} = 0.9$. On the other hand, in the limit $q \ll 1$ the pseudopotential

approximation (cf. Chap. (2.1)) applies, and a trapped particle here oscillates in a potential well of depth shown in Eq. (2.1.27).

Assuming that the particle is in thermal equilibrium with the environment at temperature T, the trap depth $\overline{D}$ should be at least [51] $\overline{D} \geq 10k_BT$. Combining the thermal and equilibrium requirements, we find

$$10k_BT\frac{4r_0^2\Omega^2}{U_{RF}^2} \leq \frac{Q}{m} \leq \frac{r_0^2\Omega^2}{2U_{RF}}0.9, \tag{2.3.1}$$

where Q/m is the charge-to-mass ratio of a confined particle.

The trap thus acts like a band-pass filter for the charge-to-mass ratio of the particles launched through the trap volume.

By scanning the voltage and/or the driving frequency, we can modify the acceptance criteria of the trap. Furthermore, if we know the exact damping factor associated with the environment and its relation with q_{max} [52], the absolute value of Q/m of a trapped object can be experimentally evaluated by increasing U_{RF} or decreasing Ω until q_{max} is reached, at which point the particles will be driven out of the trap by motional instability.

This method has been successfully used to estimate the charge-to-mass ratio of nanospheres in different configurations [53, 54].

Discussion

In this chapter we have derived the basic working principle of a Paul trap driven with one frequency. Then we have extended the derivation to the case of two frequencies in order to optimize the confinement for two different species with a charge-to-mass ratios that differ by six orders of magnitude.

The goal of the experiment consists of a silica nanosphere trapped together with a single calcium ion within the same Paul trap. Next, the addition of an optical cavity, with the trapped particles aligned along its axis, will form the optomechanical system (cf. Chap. (1)).

At the beginning of this project, however, I started with an empty laboratory with no equipment.

Taking into account the complexity and the expected time to realize a typical ion-trap experiment(see for example [55]), we decided that the fastest way to verify the two-frequency trapping scheme would be to use a simpler, rescaled physical system composed of a nanosphere and a microsphere, instead of a single atomic ion and a nanosphere, as the physics described above just depends on charge-to-mass ratios and not on actual masses.

The following chapters will thus be devoted to showing how stable trapping in a Paul trap of both a nanosphere and a microsphere have been obtained in an air environment.

Chapter 3

Experimental apparatus

A theoretical framework on ion trapping has been presented in the last section. In this chapter, the experimental apparatus will be introduced.
First, the design, fabrication and assembly of the Paul trap are presented. Second, a description of the silica nano- and microspheres used as samples in our experiment will be given. Third, the different methods to load particles into the trap will be presented. The last part of the chapter will be devoted to particle detection, using both an interferometric scheme and direct imaging of the scattered light.

3.1 The linear Paul trap realization

3.1.1 Design and fabrication

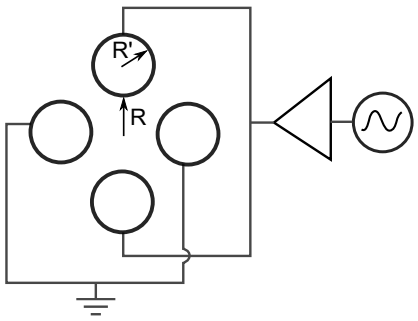

Figure 3.1: Section view of the four-rod Paul trap. Two diametrically opposed cylindrical electrodes (with radius R' separated by a distance $2R$) are connected to the RF source, while the remaining two are grounded through the optical table.

In Fig. (3.1) the general idea of the trap is sketched based on a simple quadrupole mass filter: two dielectric holders support four cylindrical electrodes for radial confinement and two additional smaller rods placed as end caps for axial confinement.

Three additional rods are included, to which DC voltages can be applied in order to compensate for stray electric fields that can displace the particle from the RF minimum, causing excess micromotion. These rods are known as compensation electrodes.

Holders

All of the trap' electrodes are fitted in the dielectric holders, which the only parts that required custom design and fabrication.

The holder is a dielectric slab with holes that match the electrodes' diameters. It keeps the electrodes parallel while ensuring the stability of the trap and providing a clamping mechanism for the system.

The design of the holder is shown in Fig. (3.2). Given the fixed radius of the rods (R'), the separation of

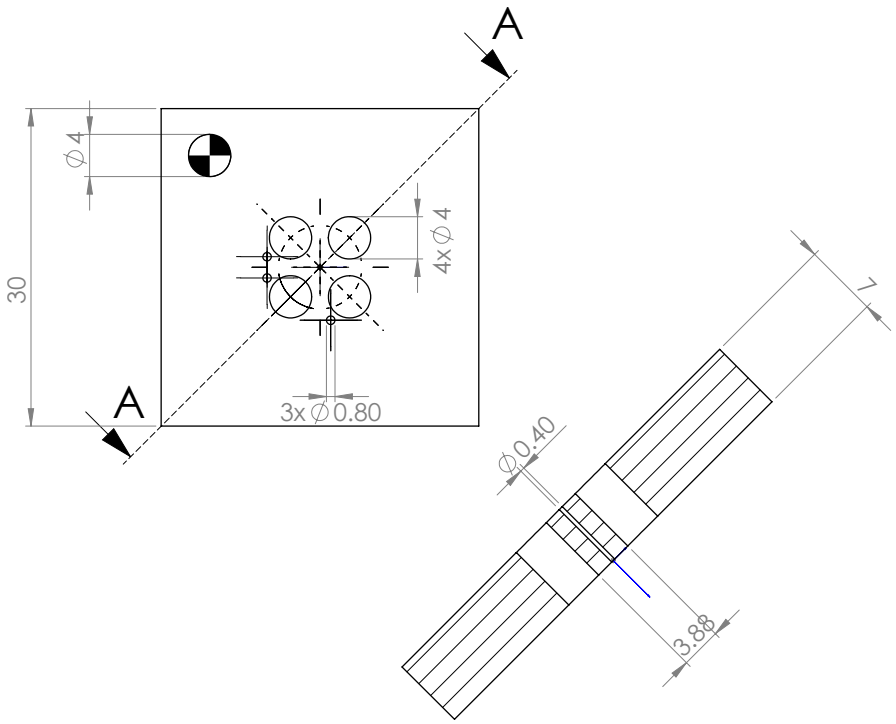

Figure 3.2: CAD drawing of one of the two identical holders for the Paul trap. All lengths are expressed in mm. The holes are: four 4 mm diameter holes for RF/ground electrodes; one 0.4 mm diameter center hole for the endcap electrode; two M4 threaded holes to accommodate screw connections with a post; three additional 0.8 mm diameter holes for compensation electrodes.

the electrodes (R) was chosen according to reference [56] and is shown in Fig (3.1)

$$R' = 1.03R. \tag{3.1.1}$$

The electric field profile arising from this geometrical arrangement of electrodes has been studied through finite element simulations[1]. For these simulations, the pseudopotential $\varphi_{pseudo}(x, y)$ can be written as [57]

$$\varphi_{pseudo}(x, y) = \frac{Q}{4m\Omega_{drive}^2}|E(x, y)|^2 \tag{3.1.2}$$

where Q and m are respectively the charge and the mass of the trapped particle and Ω_{drive} is the drive frequency of the trap. The confining potential will be harmonic only within the region where the square of the electric field depends quadratically on the radial coordinates x and y. This occurs for distances from the center of the trap less then $\sim 0.4\,\text{mm}$, as determined from the simulations shown in Fig. (3.3). A ratio

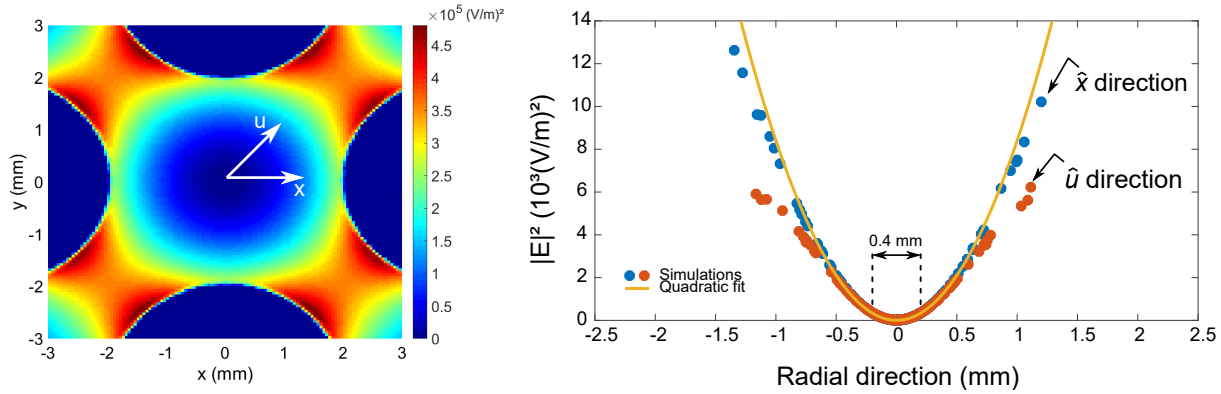

(a) **(b)**

Figure 3.3: Electrostatic simulations of $|E|^2$ arising from the geometrical configuration of Eq. (3.1.1), with 1 V applied on the two RF rods. The resulting pesudopotential can obtained with the help of Eq. (3.1.2). Figure (a) shows a contour plot of $|E|^2$ on the z=0 plane. It can be seen how the radial symmetry manifests itself just near the center of the trap. Figure (b) shows that radial symmetry is achieved within a radius of $\sim 0.2\,\text{mm}$ from the center. Below that distance, a multipole expansion fit showed that anharmonic terms became smaller than $\sim 1\%$ of the quadratic term.

of $R'/R = 1.147$ would have led to a larger area of harmonicity of the trap [58]. However, this would have implied a shorter distance between the cylindrical electrodes, compromising the fabrication process for the holder holes, and the optical access for imaging detection.

The holders have been fabricated with a precision of $\pm 0.02\,\text{mm}$ by the mechanical workshop of the University of Innsbruck's Institute for Experimental Physics.

The holders are made of polyoxymethylene (POM). POM is a polymer able to sustain up to $15\,\text{kV}\,\text{mm}^{-1}$ DC fields before dielectric breakdown [59]. We have never encountered breakdown problems while working between DC and 30 kHz and voltages applied to the rods (minimum separation of 1.5 mm) up to 1 kV.

[1] Comsol Multiphysics

Electrodes

The electrodes were made from commercially available components.

The four RF electrodes (RF and ground, see Fig. (2.2)) are stainless steel assembly rods of a commercial cage system[2], 4 mm in diameter and 50 mm in length.

The endcap electrodes are dialysis needles made of stainless, chromium-nickel steel[3], 0.4 mm in diameter and 25 mm in length. Three additional needles, 0.8 mm in diameter and 120 mm in length, were used as compensation electrodes.

Position of endcaps and compensation electrodes

The endcaps are placed in the center of the RF and ground electrode holes.

In order to minimize the distortion of the quadrupole field potential, the compensation electrodes are smaller than the RF and ground rods and they are positioned further from the center.

Trap assembly

Fig. (3.4) shows the final form of the trap.

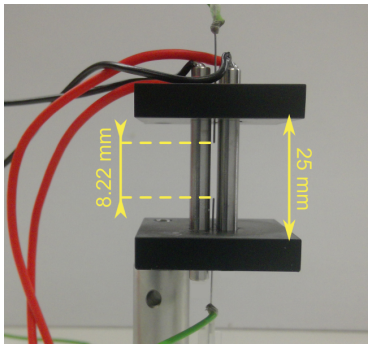

Figure 3.4: The trap assembled in vertical configuration. The bottom holder is clamped via an M4 screw to a post and is 25 mm away from the top holder. The endcap separation is 8.22 mm.

An M4 threaded hole was machined on the holder in order to clamp the assembled trap to its mount and align the trap on the optical table using standard optomechanical components.

The electrodes are tightly fit into the holder by pressure, allowing the separation of the endcaps to be regulated manually. This also makes it easier to unmount and remount the trap for cleaning. After several particles' loading sessions, in fact, the electrodes became dirt with the particle's solution (a detailed loading mechanisms description is given in Sec. 3.2).

Each electrode is connected to its power source via cables directly soldered onto it. The trap is mounted via a post to a one-axis translation stage can be finely adjusted (see Fig. (3.5)) so that its lateral position

[2] ThorLabs SR2

[3] Braun

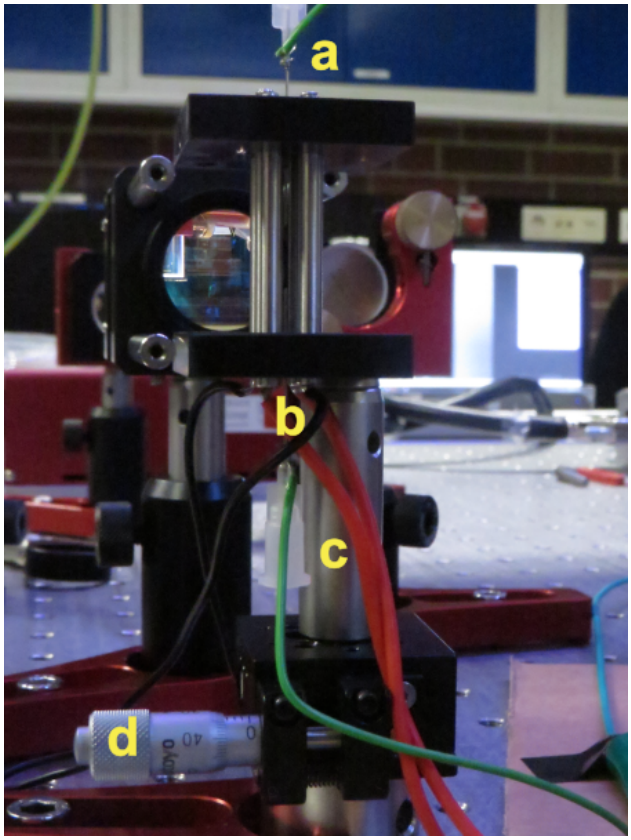

Figure 3.5: Trap mounted on the optical table. The electrical connections of the electrodes are **a)** for the top endcap (green wire) and **b)** for the bottom one (green wire) as well as the rods (red wires for the RF and black for GND). The bottom holder is fixed via an M4 screw to a post **c)**, which is clamped to a linear translation stage **d)** for alignment of the trap with respect to the detection laser beam.

with respect the detection laser beam (cf. Chap. (3.3)). A Plexiglas box covers the whole trap, protecting it from air flow.

3.1.2 Driving the trap

As described in Chap. (2), the Paul trap needs to be driven by a combination of AC and DC fields.

DC source

The endcaps and compensation electrodes are driven by DC fields. This static voltage is generated by a high precision HV module[4](Iseg box) which can provide up to ±6 kV with low current (a fraction of a

[4]EHS 60x from Iseg

microampere).

AC source

As shown in Fig. (3.1), the RF rods across from one another are driven with the same AC voltage. The ground electrodes are grounded to the table.

The RF field is generated by an arbitrary waveform generator (AWG)[5] and then amplified by a voltage amplifier[6]. The AWG has two independent outputs that give a maximum of $5\,V^{pp}$ per channel when both are switched on and $10\,V^{pp}$ if just one is used.

The amplifier can reach a maximum amplitude of 1.4 kV DC or AC, with an output current range from 0 to ± 50 mA. The maximum output voltage depends on the capacitive coupling obtained with the trap. The gain of the amplifier is tunable with a knob up to 300. The input channel supports up to $20\,V^{pp}$ AC. To match the load impedance of the trap, the dynamic adjustment knob located on the front panel of the amplifier is used.

The output is monitored with a voltage divider that gives 1/200th of the output signal.

A power splitter was used in order to feed the amplifier (which has just one input) with the sum of two RF fields, allowing us to investigate the behavior of the trap driven by two frequencies.

Remote control system

Due to the number of control knobs in the experiment and the fact that high voltage is involved, it is useful to control the experiment hardware remotely. In our experiment, this is done with the Trapped Ion Control Software (TrICS).

TrICS is developed by the Quantum Optics and Spectroscopy Group of the University of Innsbruck, and allows users to control different hardware devices via their specific libraries or through an user API.

3.2 Particle preparation and loading methods

The measurements reported here have been carried with two different sphere sizes. Hereafter we will refer to the largest ones (21.8 ± 0.9 µm from Micro particles GmbH) as *microparticles*, and to the smallest ones (0.10 ± 0.03 µm from Polysciences Inc.) as *nanoparticles*.

Both are stored as a solution (5% mass concentration) of nonporous SiO_2 in NaOH-enriched water.

The stated densities are $1.85\,g/cm^3$ for the microparticles and $2\,g/cm^3$ for the nanoparticles. With these values, the average mass of a nanoparticle and of a microparticle are estimated to be $\sim 1 \times 10^{-18}$ kg and $\sim$

[5] AFG3000C from Tektronix

[6] Trek PZD700A

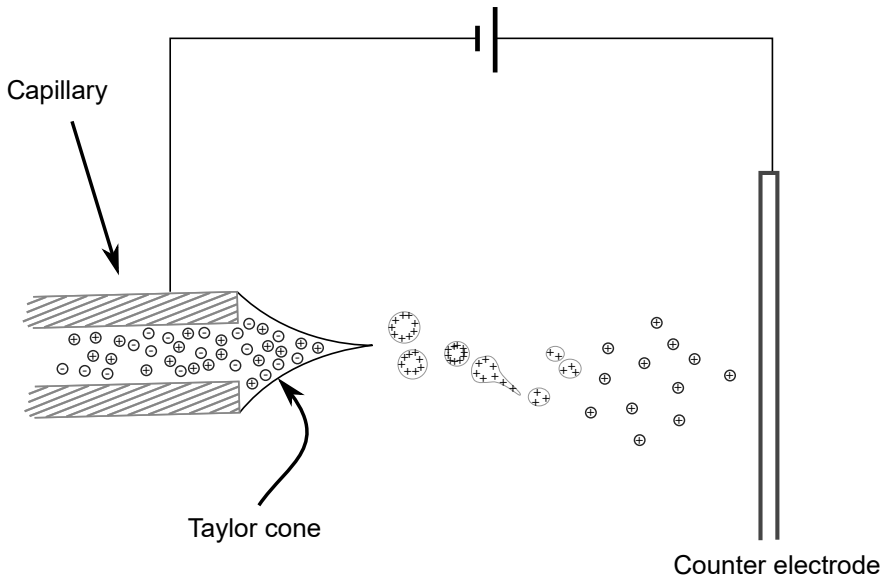

Figure 3.6: Electrospray working principle. A static voltage is applied between a capillary filled with the liquid solution and a counter electrode. When pressure is maintained on the plunger, the capillary will eject a spray of ionized particles grouped inside droplets of solvent. After the solvent has evaporated, the charged particles escape from the droplets, as they are accelerated by the electric field towards the counter electrode

1.0×10^{-11} kg, respectively.

In order to be trapped in a Paul trap, the particles need to be electrically charged and launched inside the trap's volume. For these first tests, setting up an apparatus without a vacuum chamber provides two important advantages: first, the possibility to test, in a relatively short time, several of the various trapping methods proposed in the literature, and second, the viscous damping of air, which slows the particle velocities and makes them easier to trap.

Among the schemes tested, the electrospray ionization technique turns out to be the most efficient and reproducible way of launching and charging the nanospheres. For the microspheres, a different approach is required. In the following, I will outline the basic theory behind the two methods and then explain how they have been implemented in practice.

3.2.1 Electrospray ionization of nanoparticles

Electrospary ionization (ESI) is a technique used to obtain charged particles from a liquid solution. Fig. (3.6) is depicted how ESI works. Solution is pumped through a metallic capillary needle, which is subjected to a high potential difference with respect to a counter electrode. The dissolved particles become charged via

the triboelectric effect arising from the friction between the particles and both the walls and the polarized solvent[1]. Once a certain threshold voltage is reached, the pressurized liquid exits from the needle and forms the so-called Taylor cone, named after the theoretical work of G. I. Taylor [62, 63].
A spray of droplets is observed beyond the Taylor cone. These droplets are charged, and thus they are accelerated by the electric field toward the counter electrode. In the meanwhile, part of the solvent in the droplets evaporates. This leads to a decrease in the droplets' volume and a subsequent increase of surface charge density. When the electrostatic pressure exceed the surface tension, the droplets break into smaller ones, with a cascade effect that stops with droplets containing a single charged nanoparticle.

Implementation in the lab

A basic ESI system has been built for loading the nanospheres into the Paul trap.
A medical syringe is fixed on a post and placed near the trap, pointing between the rods. The syringe's needle is connected via an alligator cable to the Iseg voltage source. The counter electrode is one of the two grounded rods of the trap itself. The syringe is filled with 10 µL of nanoparticle solution diluted with 0.5 mL of ethanol (this is a quite standard trick, used to obtain a faster evaporation of the solvent).
Applying little pressure by hand (enough to feed the small droplet at the tip of the syringe) and a voltage of 3 kV to the needle, a Taylor cone starts to appear (see Fig. (3.7)). Illuminating the trapping region with a collimated laser beam ($\lambda = 650$ nm), we can observe the trapped particles with naked eye (see Fig. (3.8)) and register their motion with a camera.

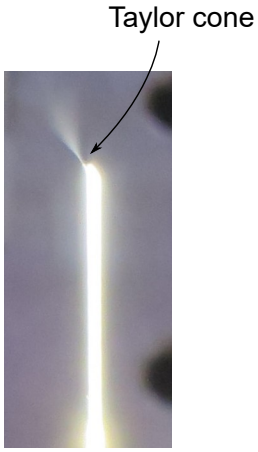

Figure 3.7: Our electrospray at work. A Taylor cone appears just after a threshold voltage of 3 kV is applied to the syringe needle.

3.2.2 Charging and launching of microparticles

After several tests, we figured out that the method used for the nanospheres does not work with the microparticles. Therefore we decided to follow a different approach.
A small volume of the microparticle solution diluted with ethanol is applied on a thin flat electrode connected to a Van de Graaff generator. The thin electrode is clamped on a post and placed close to the trap.
Once switched on, the Van de Graaff generator produces a voltage difference of hundreds of volts by accumulating charges on the thin electrode. Some of these charges become attached to

[1] It remain an open question and topic of both physics and chemistry research how ion formation actually takes place. Rayleigh discharge [60] and field-induced droplet ionization [61] are the most investigated techniques.

the surface of the dielectric spheres, which in turn are expelled from the electrode surface via electrostatic repulsion.

The difference between this method and the one used to charge the nanospheres is that the charging of microparticles is based only on the triboelectric effect, and does not involve evaporation of the solvent. Indeed, we also trapped from a dry powder of microspheres initially deposited on the tip electrode, demonstrating that friction with the electrodes is sufficient to charge the particles.

It should be noted that the presence of residual ethanol in this case is unavoidable since the microparticle solution takes a long time to dry completely ($\sim 1\,\mathrm{h}$). This turns out to be an advantage as it seems easier for the particles to become charged and expelled in a liquid emulsion than in a dry surface.

3.3 Detection schemes

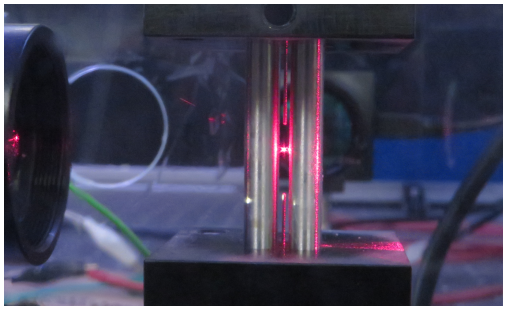

Figure 3.8: Photograph of scattered light from a trapped microsphere. A red laser beam ($\lambda \sim 650\,\mathrm{nm}$) is focused on the particle's position inside the trap. The scattered light from the particle can be seen even with naked eyes.

Even a simple LED torch is able to reveal the particles' position inside the trap. Nevertheless, we require a more accurate detection technique to obtain quantitative information about the particle motion. In our case, we are interested in the amplitude and frequency of the motion of the trapped particles. For this purpose, we have chosen to use back-focal-plane interferometry, which is characterized by high temporal and spatial resolution [64]. Moreover, we use standard imaging to detect the relative position of the particles inside the trap. The aim of this section is to present the theory and implementation of these detection schemes.

3.3.1 Laser and spatial filter

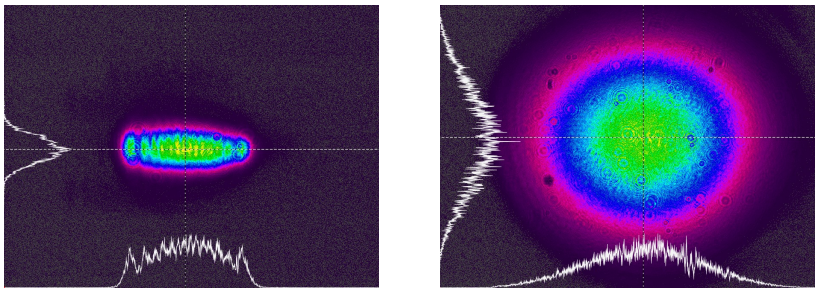

(a) **(b)**

Figure 3.9: Transverse laser mode at the input **a)** and output **b)** of the spatial filter imaged on a beam profiler. A symmetric mode is important to guarantee equal efficiency in the detection of the lateral motion of the trapped particle in both transverse directions.

The laser used to illuminate the particles is a red diode laser at 650 nm. The intensity profile at the output of the laser head is spatially multimode (see Fig. (3.9)). In order to obtain a Gaussian profile, we assembled an optical spatial filter: this consists of two lenses (f=30 mm and f=200 mm) set in a confocal configuration. At the beam focus we place a 15 µm pinhole. After the spatial filter, the laser output power is reduced from ~ 5 mW to ~ 2 mW.

3.3.2 Back-focal-plane interferometry detection

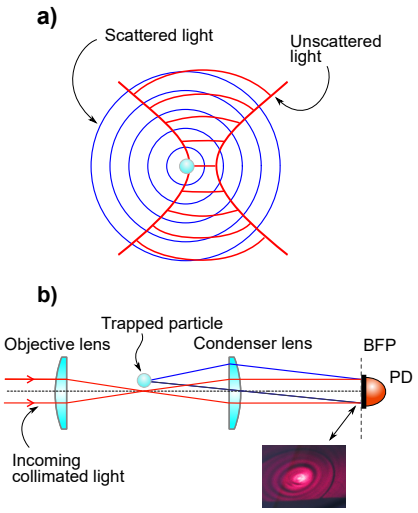

Figure 3.10: Laser light is focused on the trapped nanosphere. **a)** The unscattered light (in red) leaving the focus is shifted in phase by the Gouy phase (see text) with respect to the scattered light from the particle (in blue). **b)** The interference of the scattered and unscattered light fields is analyzed with a photodiode (PD) at the back focal plane (BFP) of a condenser lens.

Back-focal-plane (BFP) interferometry is widely used for the detection of levitating particles ranging

from nanometers to micrometers in size. This technique offers high resolution both in the time domain and spatial domain, allowing extremely precise measurements. In the optical tweezers community, for instance, it permits forces to be determined down to the piconewton scale [65] in all three dimensions [66]. This techique relies on the scattering of part of the light field illuminating the object we want to measure, and the subsequent detection of the interference pattern between scattered and unscattered light in the back focal plane of a condenser lens. A quadrant detector [67] or a position-sensitive photodiode [68] determines the intensity change of the pattern and converts it into an electric signal that is then recorded and analyzed.
The goal of this section is to give a simplified theoretical explanation of the resulting interference pattern and to show how useful information about the trapped particle's motion can be extracted from it.
The imaging beam is focused in the middle of the Paul trap, where the particle is trapped. We use a lens with a focal length of 40 mm. A fine adjustment of the focal spot is achieved by maximizing the visibility of the interference fringes in the back focal plane (see the inset in Fig. (3.10) (b)).

Interference and lateral displacement detection

BFP detection is based on the interference pattern created by a Gaussian beam and a scatterer placed at its focus. In the following, we will develop the basic tools to show the dependence of the detected signal on the particle displacement. We will first derive the equation for lateral displacement (i.e., for the case in which particle remains in the focal plane), and then for an axial displacement. The present derivation follows the work of Gittes et al. [69]. The starting point is the description of both the incoming and the scattered light field. We assume that:

1. $\lambda \gg d = 2a$, where λ is the wavelength of the laser, d is the diameter of the particle, and a is the radius of the particle.
   This is the so-called Rayleigh or electrostatic approximation, as we consider the incoming field as constant within the volume occupied by the sphere. This allows us to calculate the polarizability of the sphere within the approximation of a uniform field (see Eq. (3.3.3)).
   In our case, $\lambda = 650\,\text{nm}$. It follows that the relation $\lambda \gg d$ is only valid for the nanosphere. The case of the microsphere, where $\lambda \ll d$, requires a different approach and will be discussed later in Sec. 3.3.2.

2. The laser beam is well described as a paraxial Gaussian beam.
   The measured beam waist after the spatial filter is $w_{in} = 2\,\text{mm}$. Since the beam is focused by a $f = 40\,\text{mm}$ lens, the half angle at the focus is $\sim 2°$: thus, the small-angle approximations $\sin\theta \approx \tan\theta \approx \theta$ is reasonable.

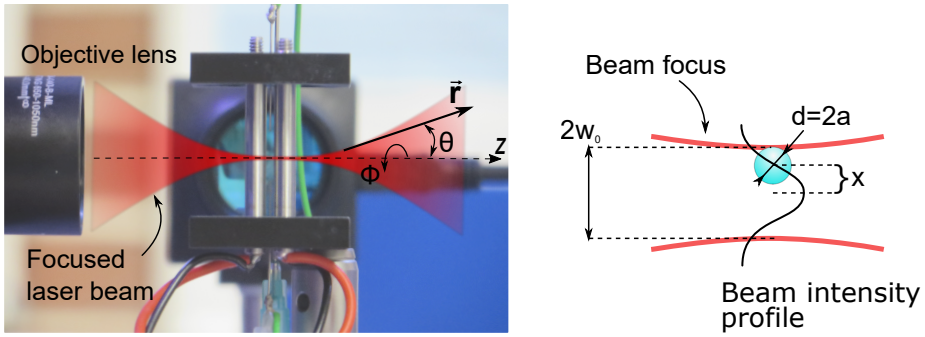

(a) light field coordinates **(b)** particle coordinates

Figure 3.11: **a)** Coordinate systems used in the text for the far electric field (photograph of the trap plus a representation of the focused beam): $\mathbf{r}$ is the distance from the focus, θ is the polar angle with respect to the optical axis z, and ϕ is the azimuth angle. **b)** Coordinate systems used for the particle lateral position: d is the particle diameter, a its radius, x its lateral displacement from the optical axis z, and w_0 is the beam waist.

Taking the beam focus as the origin of the coordinates system (see Fig. (3.11) for the definitions of the light's and the particle's coordinates), the amplitude of the unscattered beam in the far field ($r \gg w_0$) can be written as [9]:

$$E(\mathbf{r}) \approx \frac{-ikw_0 I^{1/2}}{r(\pi\epsilon_0 c)^{1/2}} \exp\big(ikr - k^2 w_0^2 \theta^2/4\big), \tag{3.3.1}$$

Here $k = 2\pi/\lambda$; ϵ_0 and c are the permittivity and the speed of light in vacuum; I is the intensity of the input beam and w_0 is the beam waist. The $-i$ factor appears due to the Gouy phase that adds an overall phase $-\pi/2$. This phase is absent in the scattered field, which is crucial for the emergence of interference.
The scattered field in the far field corresponds to a conventional dipole radiation pattern. For a small lateral displacement x, the electric field at the particle position is:

$$E(x) = \frac{2I^{1/2}}{w_0(\pi\epsilon_0 c)^1/2} \exp\big(-x^2/w_0^2\big). \tag{3.3.2}$$

This field induces a dipole moment $P = 4\pi\epsilon_0 \alpha E$ of the particle, where α is the polarizability of the sphere calculated in the static field approximation [70]

$$\alpha = a^3 \frac{n_s^2 - 1}{n_s^2 + 2}, \tag{3.3.3}$$

where n_s is the refractive index of the sphere. The induced dipole oscillates at the laser frequency, emitting a dipole radiation pattern that can be approximated in the far field as:

$$E' \approx \frac{k^2\alpha}{r}\, E(x) \exp(ik|\mathbf{r} - \mathbf{r}_s|) \approx \frac{k^2\alpha}{r}\, E(x) \exp[ik(r - x\sin\theta\cos\phi)], \tag{3.3.4}$$

where we are using the spherical coordinate system depicted in Fig. (3.11) (a).
The condenser lens collects the scattered and unscattered fields. The interference of these two fields produces an intensity difference, when compared with the unscattered field only:

$$\delta I = \frac{\epsilon_0 c}{2}[|E + E'|^2 - |E|^2] \approx \epsilon c \,\mathrm{Re}[EE'^*], \tag{3.3.5}$$

where the term $|E'|^2$ is neglected ($|E'| \ll |E|$).
By substituting Eq. ((3.3.1)), Eq. ((3.3.2)) and Eq. ((3.3.4)) into Eq. ((3.3.5)) and considering small angle θ, we obtain the relative intensity change in the back focal plane:

$$\frac{\delta I(x)}{I} \approx \frac{2k^4\alpha}{\pi r^2} x e^{-x^2/w_0^2}\ \theta\cos\phi\ e^{-k^2 w_0^2\theta^2/4}. \tag{3.3.6}$$

Equation ((3.3.6)) describes the interference pattern of the reference laser beam and the scattered light of the particle in the beam's focus and displaced by x from the optical axis, observed at angles (θ, ϕ). In the limit of small displacements ($x \ll w_0$), the intensity of the outgoing light is proportional to the particle motion along x.
A photodiode is used to traduce the light intensity in a voltage signal. The detector response is obtained integrating equation ((3.3.6)) on the sensor area. Because of the $\cos\phi$ dependency, the contribution from angles $-\pi/2 < \phi < \pi/2$ cancels with the contribution from $\pi/2 < \phi < -\pi/2$. Therefore is convenient to split the integrated intensity into $\delta I = \delta I_+ + \delta I_-$, with

$$\frac{\delta I_\pm}{I} = r^2 \int_{\mp\pi/2}^{\pm\pi/2} d\phi \int_0^{\theta_{max}} \delta I(x) \sin\theta d\theta. \tag{3.3.7}$$

Experimentally this is achieved by placing a D-shaped mirror after the condenser lens, oriented in such a way that the beam is divided in two halves, each of which will be detected by an identical photodiode. Then, subtracting the signal of one photodiode from the other (balanced configuration) we obtain the signal corresponding to $\delta I_+ - \delta I_-$. In this way, when $x > 0$ (Fig. (3.12) left) one photodiode measures the positive lobe of the interference, while the other measures the negative one. The situation is inverted when $x < 0$ (Fig. (3.12) right). Fig. (3.13) shows the relationship between the coordinates used in this chapter and the ones of the Chap. 2 used for describing the motion in the Paul trap.

Thanks to the simplifications made so far, it is possible to get an explicit analytic solution [67] for the response of the photodiode. For condenser optics with a low numerical aperture, the paraxial approximation gives

$$\frac{\delta I_+ - \delta I_-}{I} \cong \frac{16}{\sqrt{\pi}} \frac{k\alpha}{w_0^2} G\left(\frac{x}{w_0}\right) \tag{3.3.8}$$

where $G(u) = e^{-2u^2} \int_0^u e^{-y^2} dy$. The quantity $(\delta I_+ - \delta I_-)/I$ is plotted in the left part of Fig. (3.14) as a function of the lateral displacement x. The difference in voltage between the photodiodes exhibits a linear

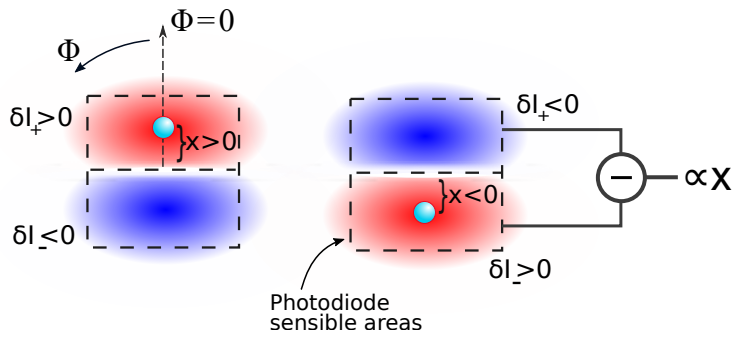

Figure 3.12: When the nanosphere is displaced by $x > 0$ (left figure), the scattered light intensity relative to the incoming laser beam on the upper half δI_+ is positive, while is negative for the lower half. The situation is inverted when the particle is displaced by $x < 0$ (right figure). The difference between the upper and lower intensity patterns can be converted into a voltage signal by a vertical split photodiode (dashed line) aligned with the optical axis, giving a direct measure of the lateral nanosphere displacement.

behavior near $x = 0$ with a slope proportional to $\sim \frac{d^3}{\lambda w_0^3}$.
This linear regime holds for lateral displacements up to approximately $\sqrt{2}w_0$. For larger lateral displacements, the intensity of the field scattered by the particle decreases as $E \sim e^{-(x/w_0)^2}$.

Axial displacement detection

When the particle moves along the optical axis z, it will experience a field [9]

$$E(\mathbf{r}_s) = E(z) = \frac{2I^{1/2}}{w(z)(\pi\epsilon_0 c)^{1/2}} \exp(-ikz + i\zeta(z)), \tag{3.3.9}$$

where $z_0 = \pi w_0^2/\lambda$ is the Rayleigh length, $w(z) = w_0\sqrt{1 + (z/z_0)^2}$ and $\zeta(z) = \arctan(z/z_0)$. We proceed now as we did for the lateral displacement, substituting Eq. (3.3.9) both in the expression for the induced dipole moment and for the scattered field Eq. ((3.3.4)), always in the far-field regime.
We thus obtain a relative intensity change in the back focal plane due to the presence of a particle [71]:

$$\frac{\delta I(z)}{I} = \frac{2k^3\alpha}{4\pi^2\epsilon_0 r^2} \sin(kz + \arctan(\zeta)) \cos\theta \exp\left(-k^2 w_0^2 \theta^2/4\right) \approx \frac{2k^4\alpha z}{4\pi^2\epsilon_0 r^2} \cos\theta \exp\left(-k^2 w_0^2 \theta^2/4\right), \tag{3.3.10}$$

where the last linear approximation holds for $z \approx 0$. Note that $\delta I(z)$ here no longer depends on the azimuthal angle ϕ.

The right part of Fig. (3.14) shows the relative detector response versus the axial displacement z.
For the parameters chosen in the experiment, $w_0 \approx 4\,\mu\text{m}$ and $z_0 \approx 80\,\mu\text{m}$, the sensitivity of the lateral displacement is $\sim$ one order of magnitude higher than the sensitivity of the axial displacement.

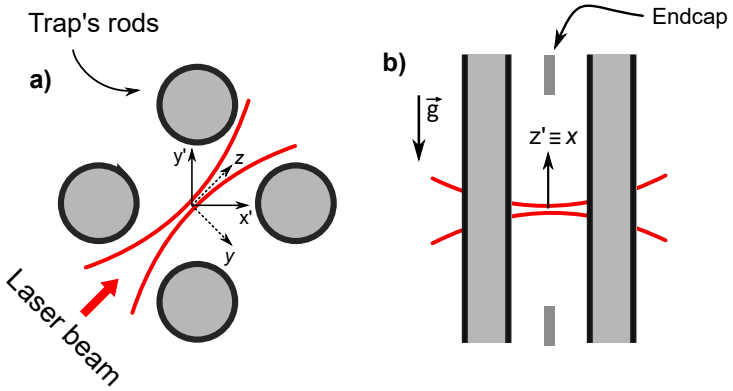

Figure 3.13: Relationship between the orthogonal coordinates $\{x', y', z'\}$ used for describing particle motion in the Paul trap as used in Chap. 2, and the particle detection system coordinates $\{x, y, z\}$. **a)** A section view;**b)** a lateral view of the relative position of the detection beam and the Paul trap.

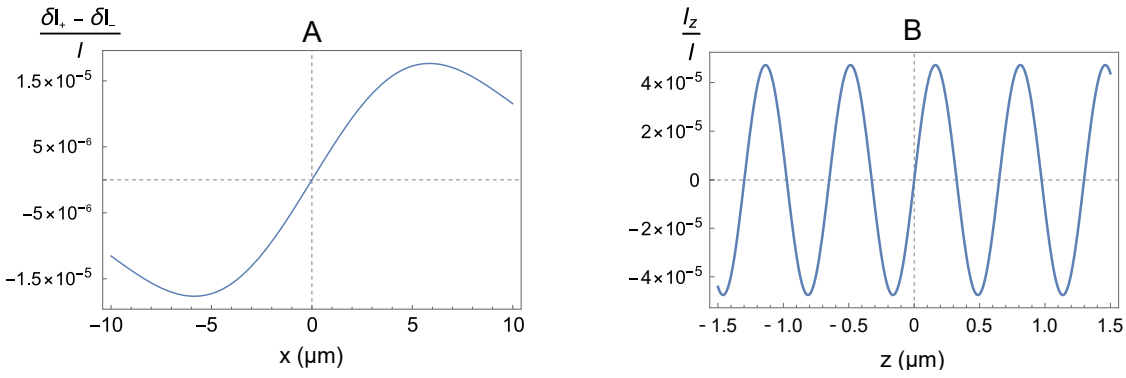

Figure 3.14: Relative detector response for lateral (**A**) and axial (**B**) particle displacements obtained within the paraxial approximation. The plots were obtained for a 100 nm diameter particle in a 650 nm laser beam with an incoming beam waist of $w_0 = 2\,\text{mm}$ focused with a $f = 40\,\text{mm}$ lens.

Back focal plane detection of microparticle motion

As the microsphere has a diameter of $d = 21\,\mu m \gg \lambda$, it cannot be considered under the Rayleigh approximation, and to find an expression for the scattered fields, one should find the Mie scattering term [15]. Fortunately, this regime ($d \gg \lambda$) allow us to use a simple ray optics picture [51, 72] in order to see how the incoming rays focused by the lens are deflected by the microsphere and how the photodiode's response relates to the particle movement. For a positive lateral displacement of the microparticle (Fig. (3.15)), the

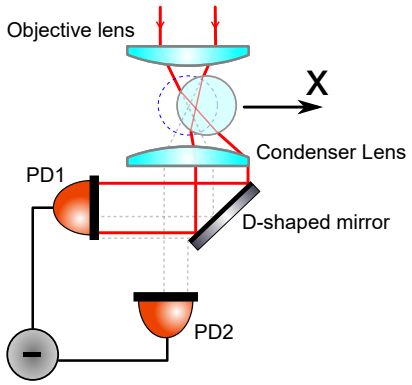

Figure 3.15: When the microsphere is laterally displaced from the optical axis, it deflects the incoming laser beam. A D-shaped mirror can distribute the deflected light to a pair of photodiodes (PD1 and PD2). The difference of the signals detected at the photodiodes gives a direct measurement of the lateral particle displacement x.

incoming light is mostly deflected towards the first photodiode (PD1). On the other hand, when the particle moves to the left of the optical axis, the majority of the light follows a straight path to the second photodiode (PD2). Therefore, the difference of the signals PD1-PD2 encodes the lateral motion x of the microsphere.

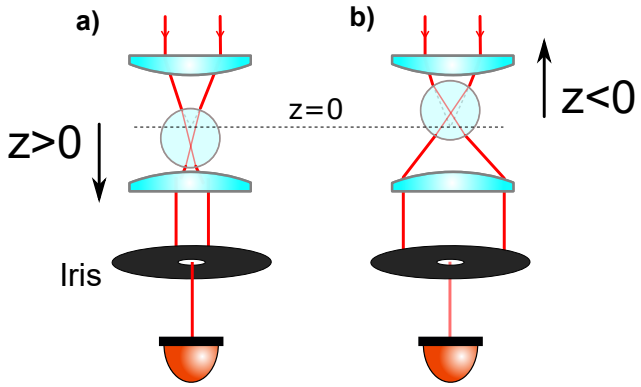

Figure 3.16: Axial displacements of the microsphere shift the detection beam focus, changing the outgoing beam collimation. The figure shows positive (**a**) and negative (**b**) displacement of the particle in the axial (z) direction. An iris placed after the condenser lens filters the amount of light detected by the photodiode, which gives a signal proportional to the particle axial position along.

Fig. (3.16) depicts the case of displacement along the optical axis. The focus in the absence of the particle lies on the plane $z = 0$. When the particle moves below it ($z > 0$, Fig. (3.16) (a)), the focus is

shifted in the same direction and light emerges out of the particle with a smaller divergence. As consequence, the collimated beam after the condenser lens gets smaller in diameter. In a similar way, for displacements in the opposite direction ($z < 0$, Fig. (3.16) (b)) we obtain a collimated beam with a larger diameter. An iris placed after the condenser lens blocks part of the collimated beam. In this way, the intensity of the light reaching the photodiode is larger when the particle is at $z > 0$ and lower for $z < 0$. Therefore, the total intensity of the light at the photodiode in Fig. (3.16) is proportional to the particle's displacement along the optical axis.

Since axial detection is based on the blockade of the outer part of the collimated beam, the more the aperture of the iris is reduced, the higher the sensitivity. Conversely, lateral detection takes advantage of the outermost part of the beam. As a result, for large particles it can also be convenient to split the signal into different detectors.

3.3.3 Camera detection

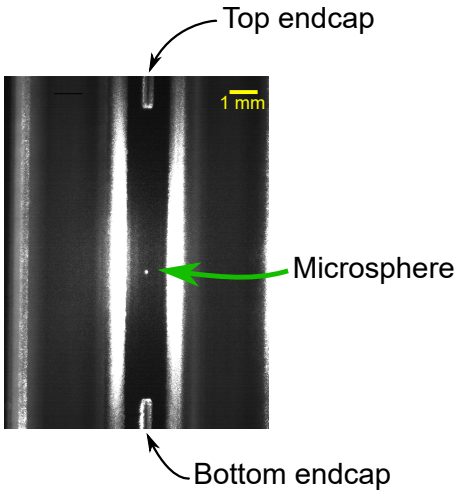

Figure 3.17: Image of a trapped microsphere taken with the CMOS camera with a resolution of 1024x1024 pixels.

In addition to interferometric measurements, we used a CMOS camera[7] to detect the position of the particles inside the trap. A typical image of a trapped particle taken with the camera is shown in Fig. (3.17). The camera is able to detect both nanospheres and microspheres. A nanosphere's image typically extends for ~ 3 pixels, a microsphere is ~ 18 pixels in diameter instead (see Fig. (3.18)). In order to optimize the image quality, various settings of the sensor, including pixel rate (up to 41 MHz), exposure time and frames per second (up to 250 fps), are adjusted via the software of the camera.

[7] DCC1545M from Thorlabs

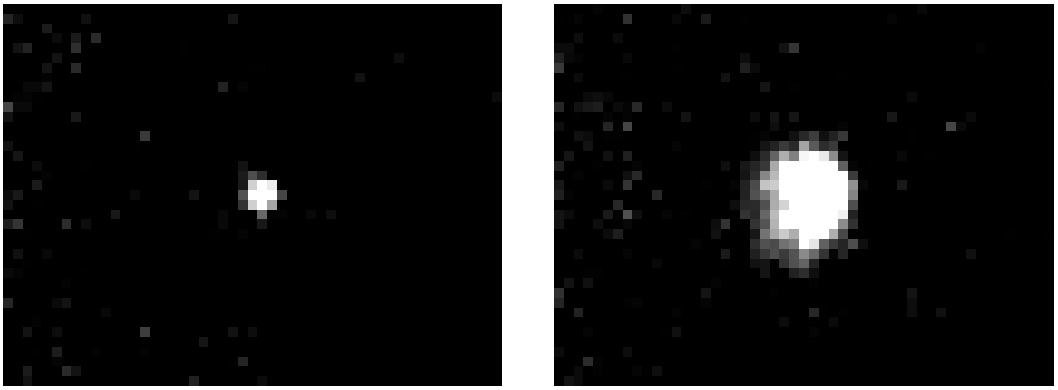

(a) **(b)**

Figure 3.18: Nanosphere (**a**) and microsphere (**b**) scattered light recorded with the camera. For a comparison of their effective sizes, these images were taken with the same camera settings (exposure time, pixel rate, intensity gain, resolution).

Since the trap is mounted in the vertical position, the two orthogonal directions for optical access both lie on the table's plane. The camera was thus placed in the direction perpendicular to the laser beam (Fig. (3.19)), given that the principal axis is used for interferometric measurements with the photodiodes.

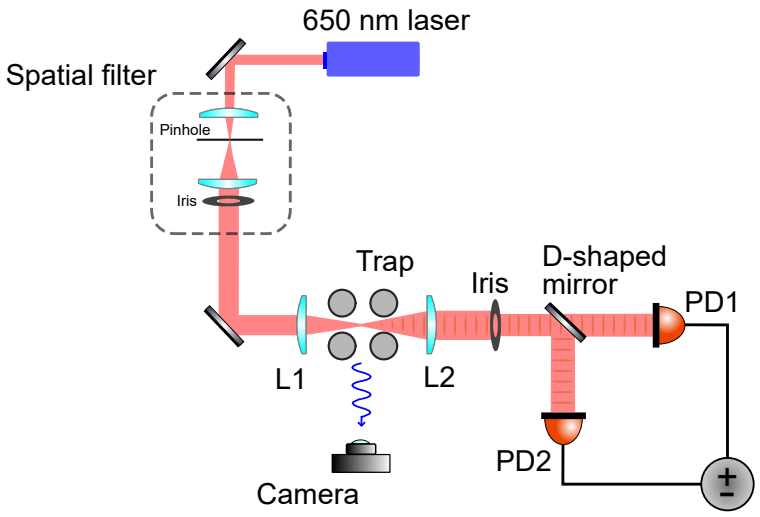

Figure 3.19: Schematic of the entire setup. The 650 nm laser for imaging enters in the spatial filter that select the TEM_{00} mode only. Then, the light is focused by the objective lens (L1) into the trapped particle. The scattered light from the particle is collected by the camera, which is placed at right angle with respect to the optical axis at the same altitude of the Paul trap. The sum of the scattered and the unscattered light is collimated by the condenser lens (L2), and then equally splitted by a D-shaped mirror. Each of the two beams leaving the D-shaped mirror goes to a pair of photodiodes (PD1 and PD2), which work in balanced configuration. An iris placed before the D-shaped mirror reduce the beam's diameter, ensuring the axial motion detection of microsphere (see Sec. 3.3.2).

Distance calibration

After a proper calibration, camera detection allow us to infer the absolute equilibrium position of the trapped particle within the electric field of the Paul trap, which in turn provides useful information about the charge state of the particle (cf. Chap (4.1.1)). Fig. (3.20) shows a pixel intensity profile along the vertical axis of the trap that intersects the endcap electrodes and the trapped microsphere. The distance calibration is made possible by the known size of the endcap electrodes (diameter of 0.4 mm). In this way, we can calculate the conversion factor between pixels and millimeters C:

$$C = \frac{\text{endcap diameter in (mm)}}{\text{endcap diameter in (pixels)}} = 0.0106 \pm 0.0001\,\text{mm/pixel} \tag{3.3.11}$$

3.4 Data analysis tool

The electric signals coming from the photodiodes of the imaging system are connected to a Field Programmable Gate Array (FPGA) board[8]. The two inputs of the board sample the analog inputs at a rate

[8]Red Pitaya STEMlab 125-10 board

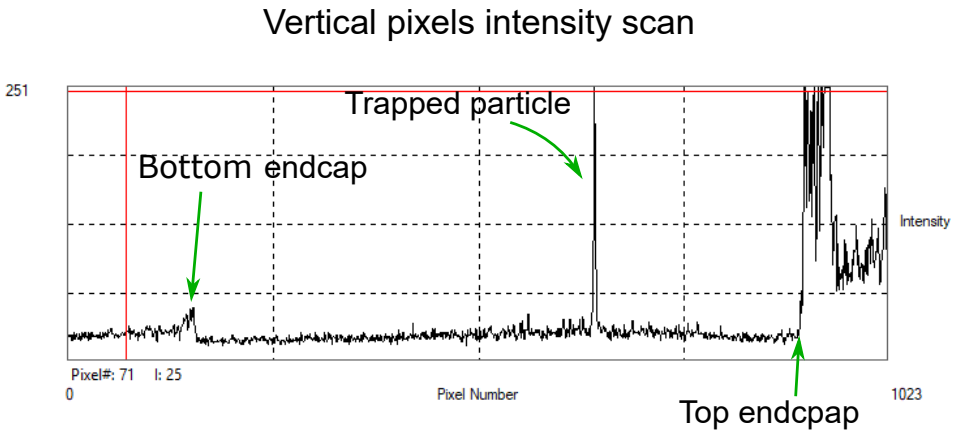

Figure 3.20: This plot shows the pixel intensity (au) as a function of the pixel position along a vertical line passing on the two endcaps. The graph is taken from the camera software.

of 125 Msps with a resolution of 14 bit; the maximum input voltage is 20 V. The card is equipped with an open-source software package that provides an oscilloscope and a spectrum analyzer [73] that we use to compute the power spectral density of the trapped particle motion.

Chapter 4

Experimental results

Once different species of charged particles can be loaded into the ion trap systematically, it becomes possible to study their motion and relate their behavior to the stability parameters.
This chapter will be devoted to showing how the quite different sizes and charges of the nanospheres and microspheres lead to a substantial difference in their motion inside the trap. Finally, an implementation of a trap driven by two different RF fields to trap the different species will be presented.

4.1 Characterization of the trap and loading methods

We first want to identify the parameters that influence the number of charges on the particles. This will allow us to find a protocol to load particles in a reproducible and systematic way.
Nanospheres are loaded using electrospray (cf. Chap. (3.2.1)). Both the electrospray launch and capture by the Paul trap act as charge filters. Particles launched by electrospray are loaded with a variable number of elementary charges depending on various factors, mainly:

- Needle voltage
- Distance between needle and trap
- Initial concentration of the solution
- Shape and dimension of the particle

After launching, a broad distribution of charged particles is accelerated toward the trap by the electric field of the needle. However, not every particle gets trapped since Eq. (2.3.1) requires that $10k_BT\frac{4r_0^2\Omega^2}{U_{RF}^2} \leq \frac{Q}{m} \leq$

$\frac{r_0^2\Omega^2}{2U_{RF}}0.9$ (for particle stability and minimum trap depth). Thus, the trap works as a charge-to-mass filter. Since it is possible to modify the trap acceptance by varying the RF field parameters, one can reconstruct the initial charge distribution of the electrospray source in terms of the trap parameters.

4.1.1 Charge over mass measurements

After loading the trap with a single species, we measure its charge-to-mass ratio by scanning the endcap voltage while monitoring the axial position of the particle with the camera. Due to its charge, the trapped particle acts as a sensor of the static electric field produced by the electrodes, positioning itself where the electric force balances the gravitational pull:

$$m\mathbf{g} = Q\mathbf{E}(z_{eq}) \tag{4.1.1}$$

where g is the gravitational acceleration constant and $\mathbf{E}(z_{eq})$ is the value of the static electric field produced by the endcap evaluated at the trap equilibrium position z_{eq}. The electric field generated within the trap has

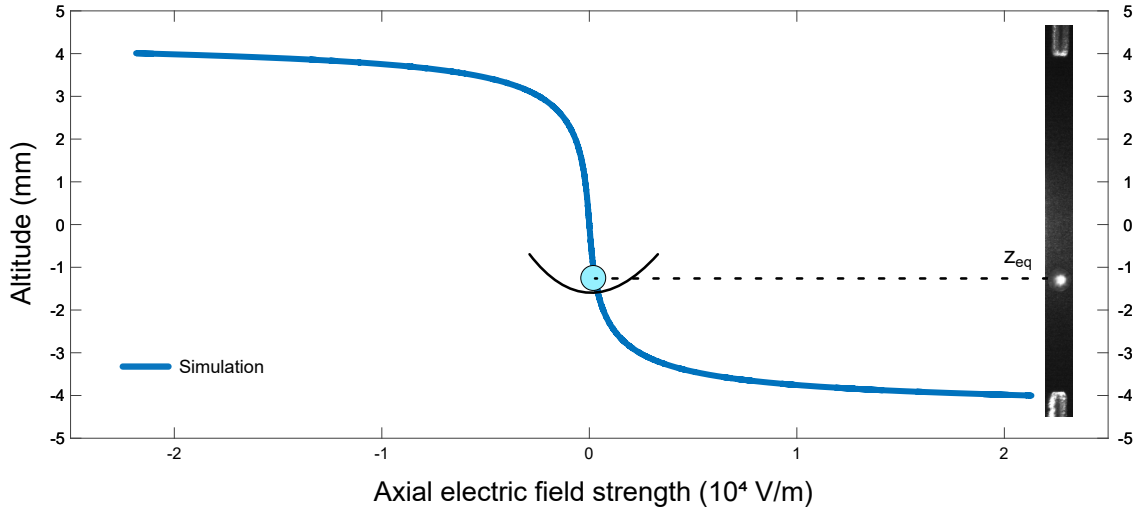

Figure 4.1: Computer simulation of the axial electric field of the trap with an endcaps voltage of 15 V.

been calculated from computer simulation[1], and it is shown in Fig. (4.1). If z_{eq} is subsequently determined from camera imaging (cf. Chap.(3.3.3)), the charge-to-mass value of single particle can be extrapolated from Eq. (4.1.1).

Charge of the microsphere

We find that our charging and launching technique (cf. Chap. (3.2.2)) can provide microparticles with

[1] Comsol Multiphysics

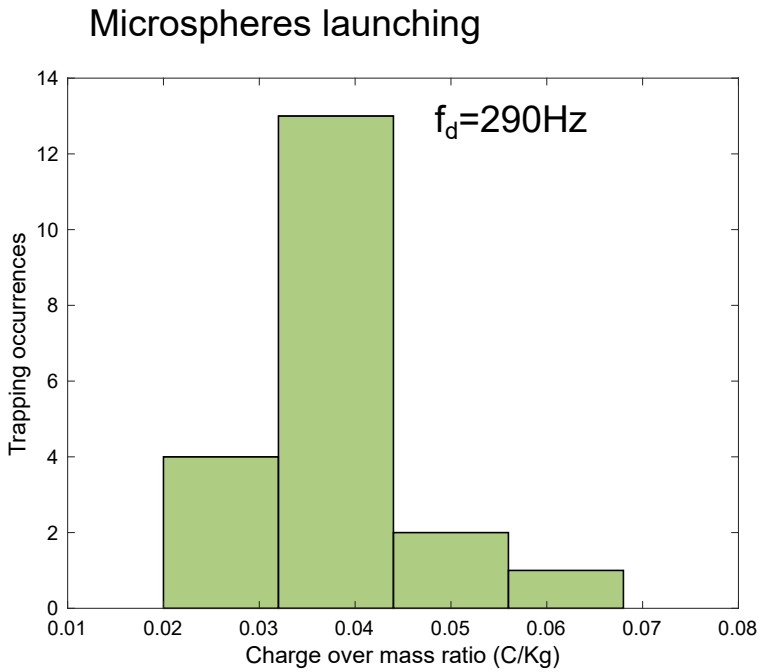

Figure 4.2: Microsphere charge-to-mass ratio distribution obtained with the Paul trap operating at the drive frequency $f_d = 290\,\mathrm{Hz}$.

a charge-to-mass ratio distributed around the value of $0.04\,\mathrm{C\,kg^{-1}}$ (see Fig. (4.2)), corresponding to$\sim 10^6$ positive elementary charges (cf. Chap (3.2) for particle volume), where the sign of the charge is manifested by the fact that particles are trapped when positive voltages are applied on the endcap electrodes.

Charge of the nanosphere

In contrast to the case of the microsphere, two distinct charge populations of nanosphere have been found from the electrospray launching technique. As depicted in Fig. (4.3), one peak of loading is observed for particles with a charge-to-mass value of $\sim 10\,\mathrm{C\,kg^{-1}}$ for trap parameters $\Omega' = 2\pi \times 2\,\mathrm{kHz}$ and $U'_{RF} \sim 800\,\mathrm{V}$. The second peak arises at the charge-to-mass value of $\sim 30\,\mathrm{C\,kg^{-1}}$ for trap parameters $\Omega'' = 2\pi \times 10\,\mathrm{kHz}$ and $U''_{RF} \sim 500\,\mathrm{V}$. Both nanosphere populations are positively charged.

To summarize, it has been found that our experimental apparatus can trap at least three well defined charge-to-mass species: one microsphere with $Q/m|_{\mu} \sim 0.04\,\mathrm{C\,kg^{-1}}$ and two nanospheres with respectively $Q/m|_{n,1} \sim 10\,\mathrm{C\,kg^{-1}}$ and $Q/m|_{n,2} \sim 30\,\mathrm{C\,kg^{-1}}$.
These charge-to-mass values are comparable with those determined from other experiments results [74, 75].

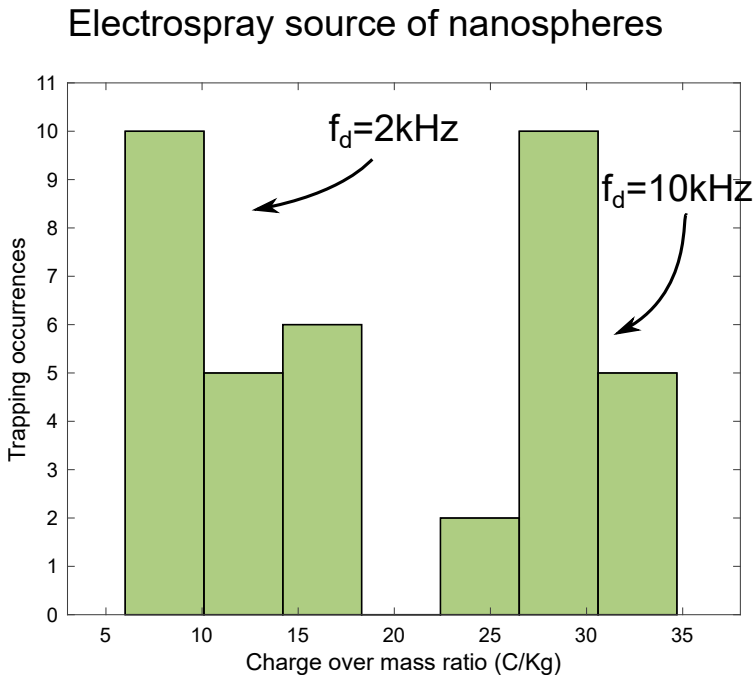

Figure 4.3: Nanosphere charge-to-mass distributions. Different drive frequencies f_d of the trap produce different populations.

4.2 Stability diagrams

To trace the boundaries of the stability diagram of our system, we study the particle motion using camera imaging (cf. Chap (3.3.3)). Fig. (4.4) shows two camera frames of a particle trapped with a different RF field in each case. As soon as the parameters of the trap (voltages U_{RF} and frequency Ω) exceed specific threshold values, a transition occurs that causes the amplitude of motion of the particle to increase. The system is said to be unstable whenever its elongated orbit start to slowly drift out of the trap. Several trapping sessions showed that after this point is reached, the chances of losing the particle increase substantially. The set of all the observed points in the parameter space that give rise to instability form the stability boundary. The nanospheres and microspheres elongated orbit's extensions close to their respectively stability boundaries is not constant in pixels number, so that the error associated with a single point in the stability diagram is estimated on a case by case basis.

The stability boundary from the $U_{RF} - \Omega$ space can be mapped into the more familiar $a - q$ space (see Chap.

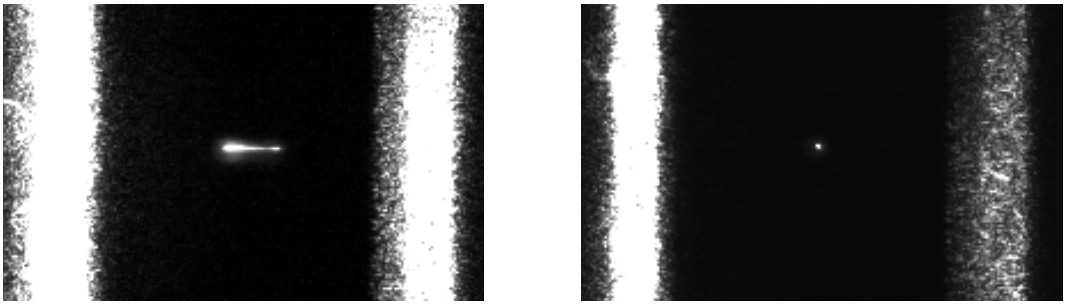

Figure 4.4: Unstable (**a**) vs. stable (**b**) motion of a microsphere inside the trap captured by the camera. The measures of voltage and frequency that label an unstable point is taken whenever the camera shows an increased orbit in pixel of about 10 times the stable case.

2) via the linear trap equations of motion. Here a and q stand for

$$\begin{aligned} a &= -\frac{4Q}{m\Omega}\left(\frac{U_{off}}{r_0^2}+\frac{U_{end}}{z_0^2}\right), \\ q &= \frac{2QU_{RF}}{mr_0^2\Omega} \end{aligned} \tag{4.2.1}$$

where U_{RF} is the AC voltage that drives the rod electrodes, which oscillates at frequency Ω; U_{end} and U_{off} are, respectively, the endcap voltage and the DC offset voltage applied to the rods; r_0 and z_0 are geometric parameters of the trap; and Q and m are the charge and the mass of the trapped particle, respectively.

In order to determine the stability diagram, the following procedure has been adopted for both nanospheres and microspheres:

1. A single particle is loaded into the trap.
2. The charge-to-mass ratio of the trapped particle is measured.
3. Starting from a stable configuration, the offset voltage of the rod electrodes U_{off} is increased until an instability is reached.
4. The offset voltage U_{off} is then lowered towards the next unstable boundary.
5. Points 3 and 4 are repeated with several different values of the driving voltage U_{RF}.

The stability diagram is then obtained by transforming the set of all the instability coordinates in the plane $U_{RF} - U_{off}$ to the aq-plane via (4.2.1).

The reason why the scanning is performed for U_{off} instead of U_{end} is that a is proportional to $\sim U_{off}/r_0^2 + U_{end}/z_0^2$: Since the endcap separation z_0 is larger than the distance r_0 between rods, a larger range of a can be covered by scanning the offset voltage rather than the axial field of the endcaps. Moreover, it has been found that the amplitude of the driving voltage accessible with our experimental setup cannot entirely cover the first stability zone (see Sec. 3.1.2 for the voltage amplifier characteristics). This problem was circumvented by adjusting the drive frequency of the trap: because of the $1/\Omega^2$ dependency of both a and q, lowering the frequency allows us to reach higher a and q values.

4.2.1 Stability diagram of the microparticle

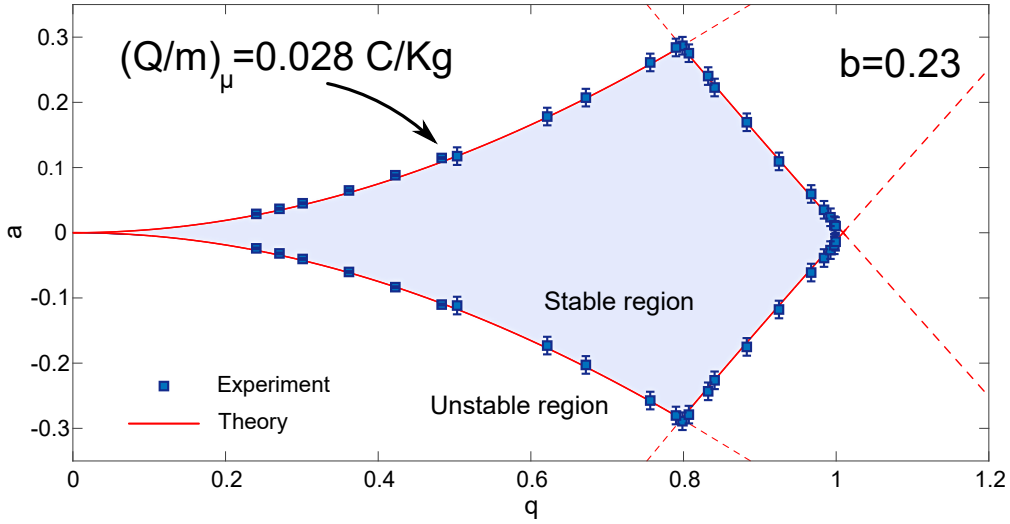

Figure 4.5: Measured stability diagram of a single $21.8 \pm 0.9\,\mu$m microsphere trapped in air at a fixed frequency $\Omega = 2\pi \times 290\,$Hz. Here the experimental data U_{off} and U_{RF} corresponding to unstable behavior were rescaled via Eq. (4.2.1) to their dimensionless parameters a and q in a way such that the charge-to-mass value of the microsphere $(Q/m)_\mu$ fits the theoretically calculated stability boundary (red solid line) for the case of trapping in air (b is obtained from Eq. (4.2.2)). For each point in the diagram, the error bar is estimated individually by observing whenever the trapped particle starts to slowly drift out of the trap. Precedent trapping sessions showed that after reaching this point the particle escapes from the trap.

The stability diagram of a trapped microsphere is depicted in Fig. (4.5). This microsphere has a measured charge-to-mass ratio of $Q/m|_\mu^{simulation} = 0.021 \pm 0.001\,\mathrm{C\,kg^{-1}}$ and was loaded and driven into

the Paul trap at the drive frequency of $\Omega = 2\pi \times 290\,\mathrm{Hz}$. The shown data are obtained from the values of U_{off} and U_{RF} corresponding to unstable behavior of the particle, then rescaled via Eq. (4.2.1) to their dimensionless parameters a and q in a way such that the charge-to-mass value of the microsphere $Q/m|_{\mu}$ fits the theoretically calculated stability case of trapping in air. For this purpose, the dimensionless damping factor b_{μ} (cf. Chap (2.1.1)) used for calculating the theoretical stability boundary has been calculated from the Stokes formula

$$b_{micro} = \frac{6\pi\eta r_p}{m_{\mu}\Omega} = 0.23 \pm 0.02 \tag{4.2.2}$$

where r_p is the radius of the particle, $\eta = 1.8 \times 10^{-5}\,\mathrm{kg\,m^{-1}\,s^{-1}}$ is the dynamic viscosity of air at ambient pressure, and the error has been calculated from the uncertainty of the particle radius (see Sec. 3.2 for a detailed description of the physical properties of the particles). A good matching between data and theoretical prediction is reached with $Q/m|_{\mu} = 0.028\,\mathrm{C\,kg^{-1}}$, confirming the goodness of the independent estimate upon the electric field simulation inside the trap.

The diagram shows the typical shape of the first region of stability, due to the overlap of the stable operation parameters in both the x and y directions (cf. Chap. 2.1). The symmetry with respect to reflection across the $a = 0$ line suggests that the same instabilities occur if we either change the polarity of U_{off} or if we apply the offset voltage to the other diagonal pair of rod electrodes. The latter is a consequence of the linear trap symmetry (cf. Chap. 2.1).

The maximum q value belonging to the stable region of air trapping in Fig.(4.5) is larger than its vacuum counterpart $q_{max}^{vacuum} \sim 0.9$. This is indeed a consequence of the air damping, which causes the enlargement of the stable region of the trap (Chap. 2.1.1).

4.2.2 Stability diagram of the nanoparticle

The stability diagram of a nanosphere with charge-to-mass ratio of $Q/m|_n^{simulation} = 10 \pm 1\,\mathrm{C\,kg^{-1}}$ trapped at $\Omega'' = 2\pi \times 10\,\mathrm{kHz}$ is shown in Fig (4.6). The nanosphere has a larger charge-to-mass value than the microsphere, which leads to the possibility to explore higher values of q. In fact, the plot never shows a closed path to a maximum q value.

Since the size of the nanospheres (radius of 50 nm) is comparable with the mean free path of air molecules at ambient pressure, $l_{mfp} = 68\,\mathrm{nm}$, kinetic theory corrections to the Stokes damping formula (4.2.2) have to be used.

According to the results of Beresnev et al. [76], the dimensionless damping parameter is given by,

$$b_{nano} = \frac{6\pi\eta r_p}{m_n\Omega}\frac{0.619}{0.619 + Kn}(1 + c_K) = 89 \pm 53 \tag{4.2.3}$$

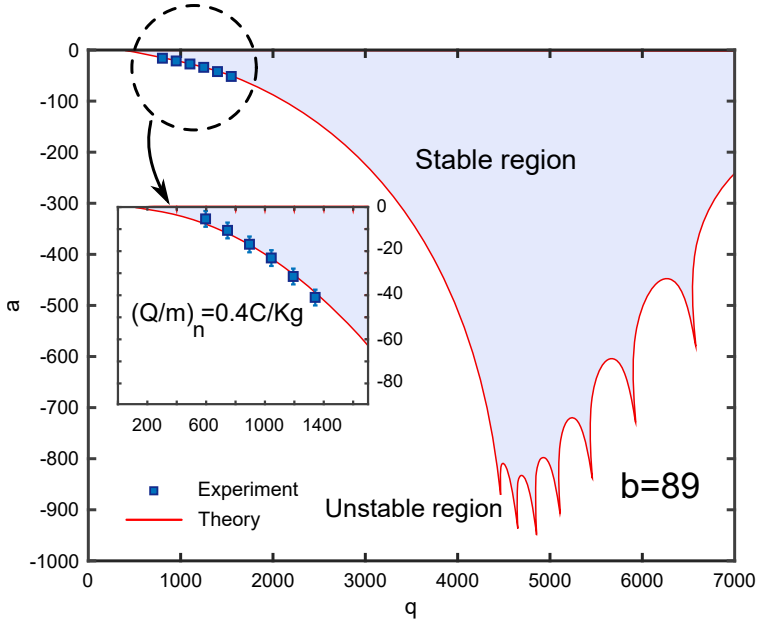

Figure 4.6: Measured stability diagram of a trapped nanosphere at frequency $\omega'' = 2\pi \times 10\,\mathrm{kHz}$. The red solid line represents a theoretical stability boundary calculated with a dimensionless damping factor $b = 89$. The experimental values of U_{off} and U_{RF} have been rescaled to their dimensionless counterparts a and q via Eq. (4.2.1), obtaining a match with the theoretical prediction by using $Q/m|_{\mathrm{n}} = 0.4\,\mathrm{C\,kg^{-1}}$.

where $Kn = l_{mfp}/r_p$ is the Knudsen number, $c_K = (0.31Kn)/(0.785 + 1.152Kn + Kn^2)$ is a small positive function of Kn, and m and r_p are the mass and the radius of the nanosphere, respectively. The very large uncertainty in b_{nano} reflects the factory declared uncertainty in nanosphere's diameter $2r_p = 0.10 \pm 0.03\,\mu\mathrm{m}$. As it was done for the microsphere case, the experimental points shown in Fig. (4.6) are rescaled in a way such that the data are superimposed with the theoretically predicted stability boundary for the case of $b_n = 89$. The match was obtained with $Q/m|_{\mathrm{n}} = 0.4\,\mathrm{C\,kg^{-1}}$, in strong disagreement with the charge-to-mass ratio calculated upon the axial electric field simulation, which doesn't need a measurement of the particle radius in order to be performed, and thus results more precise.

4.3 Power spectral density of particle motion

Secular trap frequencies can be measured through evaluation of the power spectral density (PSD) of the particle motion.

We have seen how air drag is responsible for enlarging the stability domain of the trapped particles, particularly for the nanosphere. Another effect of damping is to suppress the harmonic secular oscillations. The

dynamics of a trapped particle is therefore driven by thermal fluctuations, superimposed with the effect of the driving field, which forces the charged particle to oscillates at its frequency (micromotion).

4.3.1 Overdamped regime of the equation of motion

The equation of motion for a trapped particle in air is derived here in terms of a Langevin equation, where the surrounding thermal environment is taken into account as a source of stochastic white noise [77]. The particle therefore experiences Brownian motion in the presence of a confining potential. For a simpler derivation, we consider only the harmonic regime of the external applied potential (pseudo-potential approximation, cf. Chap (2.1)), neglecting the time-varying driving force of the trap that would lead to the ineradicable presence of micromotion [68, 78].
The equation of motion of a trapped particle along the x axis of the trap is

$$m\ddot{x}(t) + \gamma\dot{x}(t) + \kappa_x x(t) = F(t), \tag{4.3.1}$$

where $\gamma = 2m\Omega b$ is the damping coefficient, κ_x is the spring constant of the trap related to its secular frequency ω_x by $\kappa = m\omega_x^2$, and $F(t)$ is the Gaussian random force associated with the thermal environment (analogous equations for the y and z axes are obtained by replacing their secular frequency respectively). The background here has a double role: It provides damping, coming from a fluid description of the medium surrounding the particle; and it acts as a source of chaotic motion, due to the kicks that air molecules randomly give to the particle. These two aspects are linked by the fluctuation-dissipation theorem [79].
The random force $F(t)$ has moments

$$\begin{aligned} \langle F(t)\rangle &= 0, \\ \langle F(t)F(t')\rangle &= 2\gamma k_B T\delta(t-t'), \end{aligned} \tag{4.3.2}$$

where T is the room temperature and k_B is the Boltzmann constant. The average $\langle ...\rangle$ is taken over the distribution of all possible realizations of the stochastic variable $F(t)$. Since the mean effect of air drag is already considered in the term $\gamma\dot{x}$, $F(t)$ has zero average, and its strength is related to the environment temperature T by the equipartition theorem. The delta distribution in the second moment of $F(t)$ means that thermal fluctuations have no memory, i.e., that there is no correlation between impacts of air molecules and trapped particle at different times t and t' (Markov process).
In the case of ambient pressure, the small Reynolds number allows us to neglect the inertial term in Eq. (4.3.1). In this regime, the equation of motion becomes

$$\gamma\dot{x}(t) + \kappa_x x(t) = F(t). \tag{4.3.3}$$

Taking the Fourier transform of Eq. (4.3.3)

$$2\pi\gamma\Big(if + \frac{\kappa_x}{2\pi\gamma}\Big)\widetilde{x}(f) = \widetilde{F}(f), \tag{4.3.4}$$

and using the second relation of equations (4.3.2), we find the PSD of the particle motion

$$|\widetilde{x}(f)|^2 = \frac{k_B T}{2\pi^2\gamma\big(f_c^2 + f^2\big)}. \tag{4.3.5}$$

Eq. (4.3.5) is an overdamped Lorentzian with cut off frequency $f_c = \kappa_x/(2\pi\gamma)$.
Therefore, the secular frequency of the trap along the x axis is given by

$$\omega_s = \sqrt{\frac{2\pi\gamma f_c}{m}}. \tag{4.3.6}$$

4.3.2 PSD of microparticle

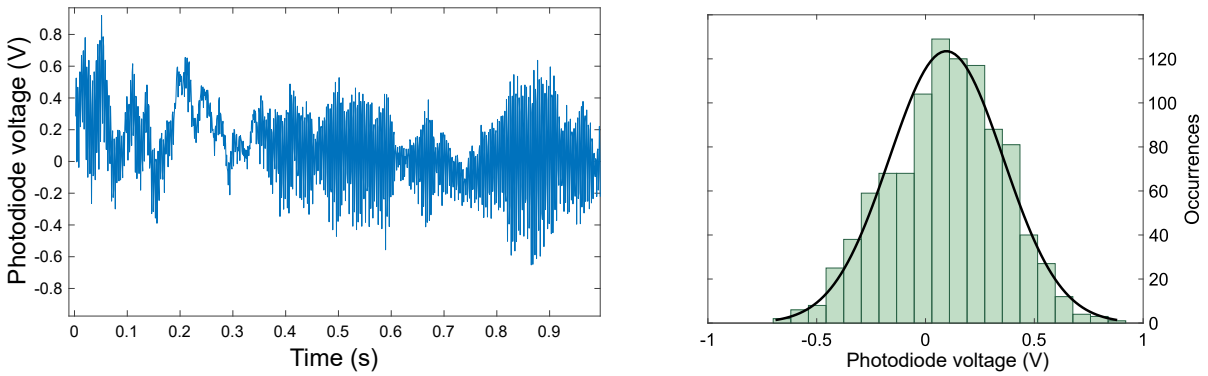

(a) **(b)**

Figure 4.7: **(a)** Experimental long-time trace of microparticle motion along the z direction (obtained with the photodiode detection, see Chap. 3.3.2) and its histogram **(b)** unveiling its Brownian particle nature. The signal from the photodiode is not calibrated for give the real particle's displacement in µm.

Interferometric back-focal-plane detection (cf. Chap.(3.3.2)) is used to obtain the PSD of nanospheres and microspheres. Fig. (4.7) (a) shows the time trace of the scattered light from a trapped microsphere reaching the photodiode. The trap is driven with a voltage of $U_{RF} = 355\,\mathrm{V_{pp}}$ at a drive frequency of $f_d = 290\,\mathrm{Hz}$. The trapped microsphere has a charge-to-mass ratio (extracted from z equilibrium position, cf. Chap. (4.1.1)) of $Q/m|_{\mu} = 0.021\,\mathrm{C\,kg^{-1}}$. With these parameters, the theoretically predicted secular frequency along the radial plane of the trap is $\omega_s^{theo} = 2\pi \times 56\,\mathrm{Hz}$.
The power spectral density extracted from the time trace of Fig. (4.7) (a) is plotted in blue dots in Fig.

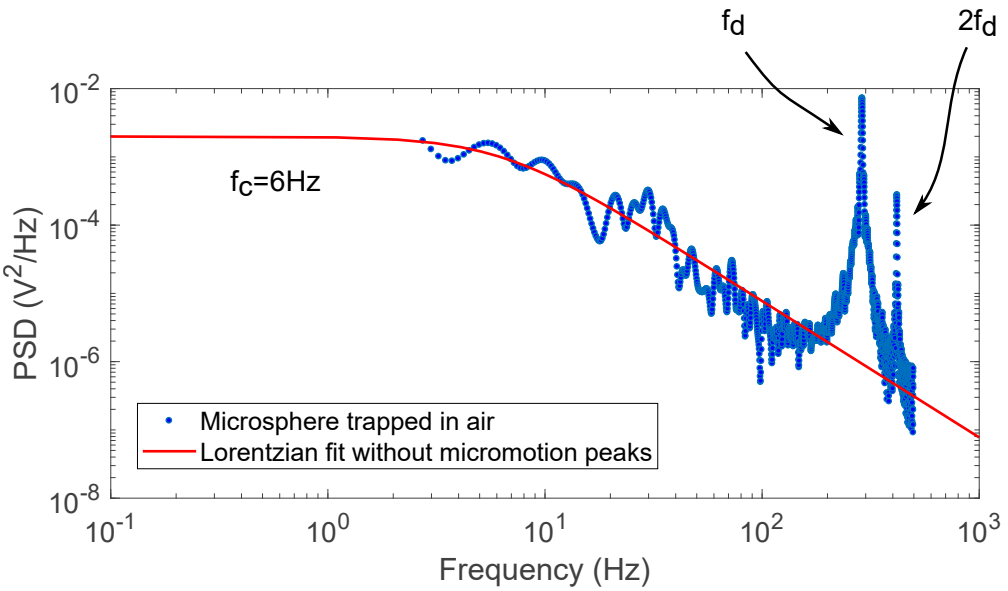

Figure 4.8: PSD of the microsphere motion (blue dots). Air drag is responsible for the disappearance of a secular frequency peak. Instead, the peaks related to the driving field frequency $f_d = 290\,\text{Hz}$ and its first harmonic at $2f_d$ are still present, suggesting the presence of micromotion. An overdamped Lorentzian fit (red solid line) with cutoff frequency $f_c = 6\,\text{Hz}$ is superimposed on the data. The fit range doesn't take into account the data set belonging to the micromotion peaks.

(4.8). The first sharp peak at $f_d = 290\,\text{Hz}$ is due to the driving field frequency. The secular frequency peak is completely absent, confirming that the motion is in the overdamped regime. Furthermore, the overdamped Lorentzian shape is almost entirely hidden by $1/f$ noise. A second harmonic is also visible at frequency $2f_d = 580\,\text{Hz}$. The appearance of this peak is most likely related with the detection scheme (cf. Chap.(3.3)): Fig. (4.9) shows how frequency artifacts could arise in the spectrum whenever the amplitude of the particle oscillations become larger than the beam transversal size, or when the beam direction itself is not well centered on the particle mean position. In fact, with a laser waist of $w_0 \sim 10\,\mu\text{m}$ (cf Chap. (3.3.2)) at the focus of the beam, even a little air movement in the neighborhood of the trap can easily push the trapped particle out of the beam, altering the computed PSD. Moreover, there are other small contributions to the second and higher harmonics of the microsphere motion from the non-ideal paraboloid shape of the pseudopotential (cf. Chap. (3.1.1)), as well as from harmonics of the carrier frequency f_d supplied by the function generator and the amplifier (the characteristics of the function generator and the amplifier will be discussed in the next section 4.4).

The limiting factor in acquiring a spectrum with sufficiently high resolution at low frequencies came from

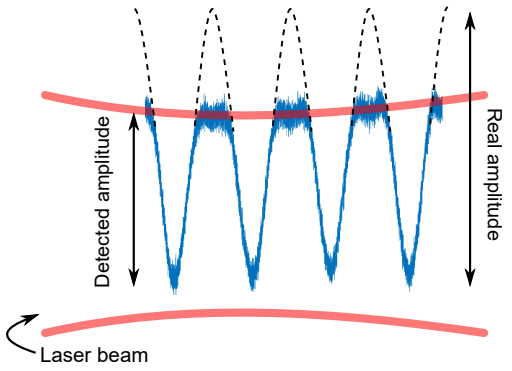

Figure 4.9: Experimental time trace of a microsphere (blue) with a superimposed sketch of the laser beam lateral profile (red). Whenever the particle motion amplitude inside the trap exceeds the detection beam size (here represented by the dashed black line), the time trace becomes truncated in amplitude, and its PSD will exhibit higher harmonics with respect to the fundamental trap frequency.

the large amount of memory needed to take a long time trace. Moreover, even small air currents present in the room can substantially affect the motion of the trapped microsphere during a long measure. In order to mitigate this problem, a plexiglas box defends the trap from the larger air flows present in the room. The red line in Fig. (4.8) is an overdamped Lorentzian fit with a cutoff frequency of $f_c = 6\,\mathrm{Hz}$. The range of frequency values used for the fit goes from 1 Hz to 200 Hz, cutting the data set related with the trap driving frequency. Substituting the found value of f_c into Eq. (4.3.6), we estimate the radial secular frequency to be $\omega_s^{meas} = 2\pi \times 20\,\mathrm{Hz}$, less than one half of ω_s^{theo}. It is common among ion trap experimentalists to treat this discrepancy between the measured and the calculated secular frequency by means of a geometrical correction factor η included in the q parameter [56, 80, 81], that now reads

$$q = \eta \frac{2QV_{rod}}{Mr_0^2\Omega^2} \tag{4.3.7}$$

This correction factor incorporates deviations from the ideal hyperbolic electrodes used in deriving the equation of motion for the trapped microsphere.
We thus obtain $\eta = \omega_s^{meas}/\omega_s^{theo} = 0.36$. However, given the problems just described above, conclusive results about trap frequencies cannot be obtained, and a more isolated environment from air seems necessary.

4.3.3 PSD of nanoparticle

The PSD of the nanosphere is plotted in Fig. (4.10). As for the case of the microsphere, the relevant peaks on the graph are due to micromotion at the drive frequency and higher harmonics. The nanosphere is trapped with a voltage of $U_{RF} = 500\,\mathrm{V_{pp}}$ at the drive frequency of $f_d = 2\,\mathrm{kHz}$.
Whenever the amplitude oscillations of the nanosphere are larger than the wavelength λ of the laser ($\lambda \sim 650\,\mathrm{nm}$), the sensitivity of the photodiode to the axial motion goes out of the linear regime (see Fig. (3.14)

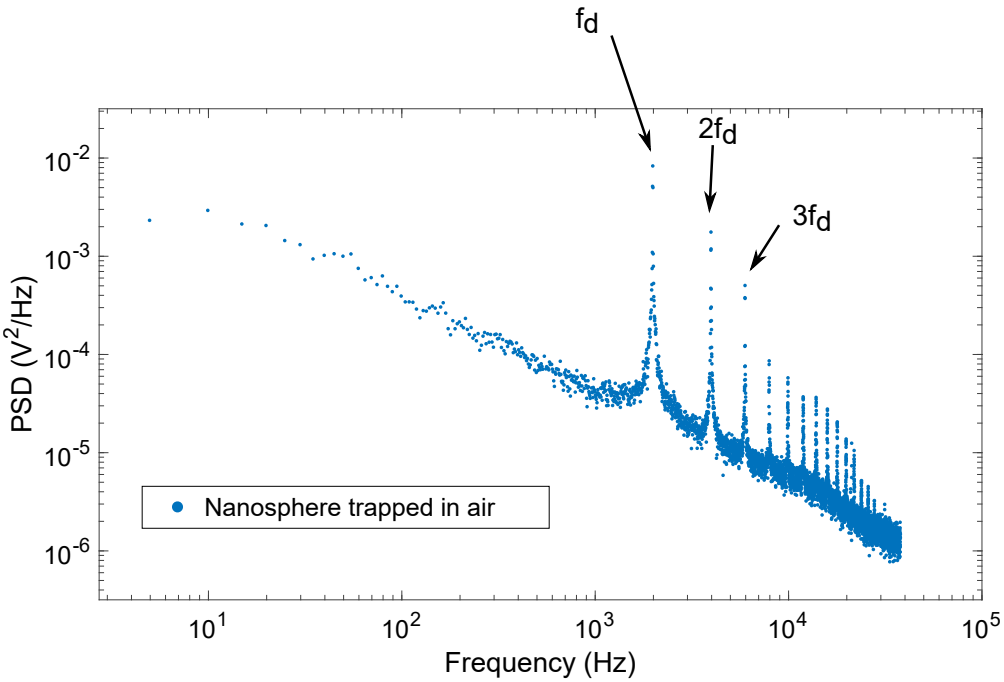

Figure 4.10: PSD of the nanosphere. The high damping of air suppresses the secular frequency of oscillation inside the Paul trap. Moreover, higher harmonics of the trapping drive frequency are present.

(b)). This leads to the appearance of higher harmonics in the axial spectrum, even if the motion is fully confined within the laser spot.

4.4 Two-particle results

The stability diagrams found in Sec. 4.2 give us the upper bounds on the voltages we can utilize in driving the trap (at fixed frequency) for confining the single species. Now it will be described how we tried to confine both species together, with the trap working with two drive frequencies. We are interested in working with just one particle per species (one nanosphere plus one microsphere), in order to work with as few degrees of freedom as possible.
Table (4.1) shows the voltages and frequencies used to individually trapping particles, and that are thus being used to drive the two frequency field.

Species	Voltage (V_{pp})	Frequency (Hz)
Microsphere	264	330
Nanosphere	800	3000

Table 4.1: Set of parameters used to trap nanosphere and microspheres together

4.4.1 Second particle loading

The following is the procedure used for loading both the microsphere and the nanosphere inside the trap:

1. A single microsphere is loaded at $f_1 = 330\,\text{Hz}$, and the value of $Q/m|_\mu$ is measured;
2. The second field at $f_2 = 3\,\text{kHz}$ is slowly switched on and ramped up to its target value;
3. The electrospray is turned on, and one or more nanospheres are trapped.

A camera shot of both species trapped together is shown in Fig. (4.11). We decided to trap the microsphere first since it behaves more stably inside the trap, and thus it can resist the flow of nanospheres coming from the electrospray (the latter is aimed as far as possible from the trapped microsphere).
Several nanoparticles are typically trapped from the loading mechanism. In order to reduce this only to one, a DC offset voltage is added to the RF rod electrodes such that some particles reach an unstable parameter zone and then leave the trap. Once the trap is populated with just a microsphere and a nanosphere, the value of $Q/m|_n$ of the latter can be estimated given the axial electric field distribution $E_z(z)$ from simulations (Fig. (4.1)) and the distance d between the nanosphere and the microsphere from camera imaging. The axial equation of motion for the nanosphere at its equilibrium position z_{eq} is

$$M_n g = Q_n E_z(z_{eq}) + \frac{Q_\mu Q_n}{4\pi\epsilon_0 d^2}, \tag{4.4.1}$$

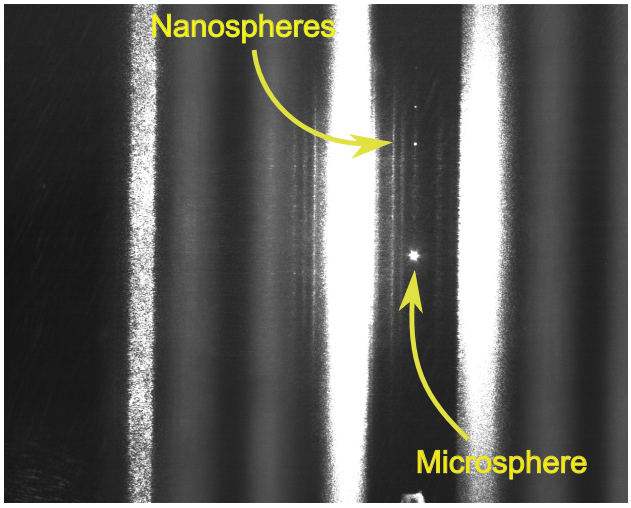

Figure 4.11: Camera image of a microsphere trapped together with multiple nanospheres. Here the Paul trap is driven with two frequencies.

where g is the gravitational acceleration, Q_μ is the charge of the microsphere obtained knowing the microsphere mass (cf. Chap. (3.2)) and ϵ_0 is the vacuum permittivity.
Solving Eq. (4.4.1) for Q/m_n, we get

$$Q/m_n = \frac{g}{\left(E_z(z_{eq}) + \frac{Q_\mu}{4\pi\epsilon_0 d^2}\right)}, \tag{4.4.2}$$

4.4.2 PSDs of particle motion

In order to obtain a PSD analysis for each species, the objective lens and the laser beam height (cf. Chap.(3.3)) are moved in such a way to address only a single particle.

Fig. (4.12) (A) shows the power spectral density of the nanosphere motion along the radial direction of the trap. The two peaks at the driving frequencies are clearly resolved. Since the PSD at f_1 is higher at f_2 than

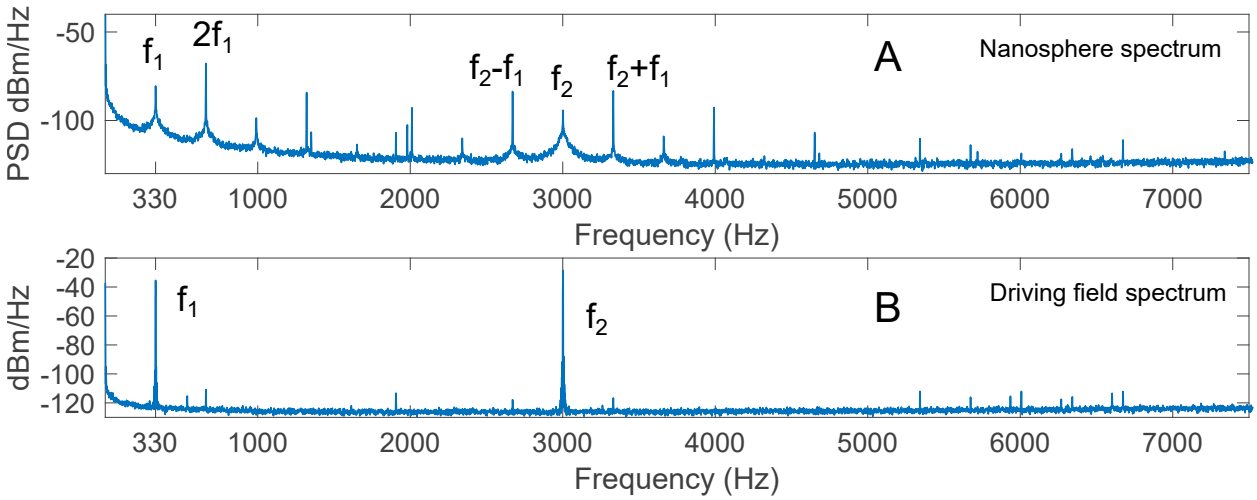

Figure 4.12: **A**: Nanosphere motion spectrum in the presence of two driving frequencies. A new feature of the graph with respect to the PSD taken with just one drive frequency (Fig. (4.10)) is the appearance of new peaks at frequencies $f_h = f_2 \pm hf_1$, with h an integer. **B**: Driving field spectrum measured from the voltage divider of the amplifier (see Sec. 3.1.2 for the voltage amplifier characteristics). The spectrum shows sidebands and other harmonics of f_1 and f_2. The suppression of the highest harmonic is $f_1 - 2f_1 = 70\,\mathrm{dBm/Hz}$).

at f_1, we can infer that the motion of the nanoparticle is mostly driven by the same low frequency originally meant to confine the heavier microsphere. In fact, after measured the PSD we switched off the fast field f_2 and observed that the nanosphere remained stably trapped, together with the microsphere. This is indeed another proof of the significant role played by air damping in the dynamics of nanosphere motion.

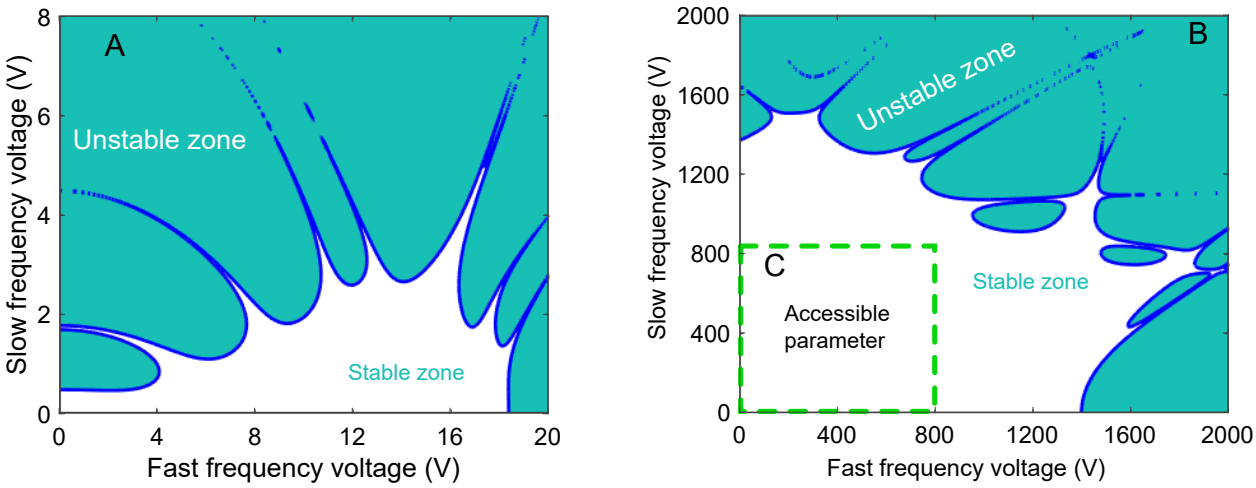

Figure 4.13: Calculated region of stability for a nanoparticle with $Q/M = 1\,\mathrm{C\,kg^{-1}}$ with $U_{off} = 0$ and trap drive frequencies f_1 and f_2. The fast frequency f_2 is set as an integer multiple of the slow frequency ($f_2 = 10 f_1 = 3.3\,\mathrm{kHz}$) for an easier evaluation of the plots. The plot in **A** is obtained with no air drag contribution ($b_1 = 0$ in Eq. (2.2.2)), while the one in **B** is calculated taking into account the presence of a background gas at air pressure ($b_1 = 269$, see Eq. (4.2.3) for the frequency dependence of b). The effect of the pressure increase leads to an enlargement of the stable operating zone of the trap. As a result, the range of voltage parameters achievable by our setup (**C**) is completely absorbed in the stable regime, where no parametric resonances can be excited.

Fig. (4.13) shows how the parametric resonance branches induced by a second frequency field are completely canceled with the high damping factor of the nanosphere at ambient pressure (cf. Chap (4.2.2)). Moreover, we have not been able to load high charged nanospheres (see Fig. (4.3)) at $f_2 = 10\,\mathrm{kHz}$. This is probably due to the fact that the slow background field already filters the flow of particles from the electrospray, resulting in an environment that is more stable for nanosphere with a low charge-to-mass ratio (see Chap 2.3 for a description on how the trap works as a charge filter).
Therefore, within the accessible range of trap parameters (cf. Chap (3.1.2)), the second frequency field is not necessary in order to stably confine the lighter particle.
The microsphere PSD is shown in Fig. (4.14). The fast field peak at $f_2 = 3\,\mathrm{kHz}$ is suppressed by $-40\,\mathrm{dBm/Hz}$ relative to the slow field peak at $f_1 = 330\,\mathrm{Hz}$, confirming that adding a second fast field has little effect on the particle motion.

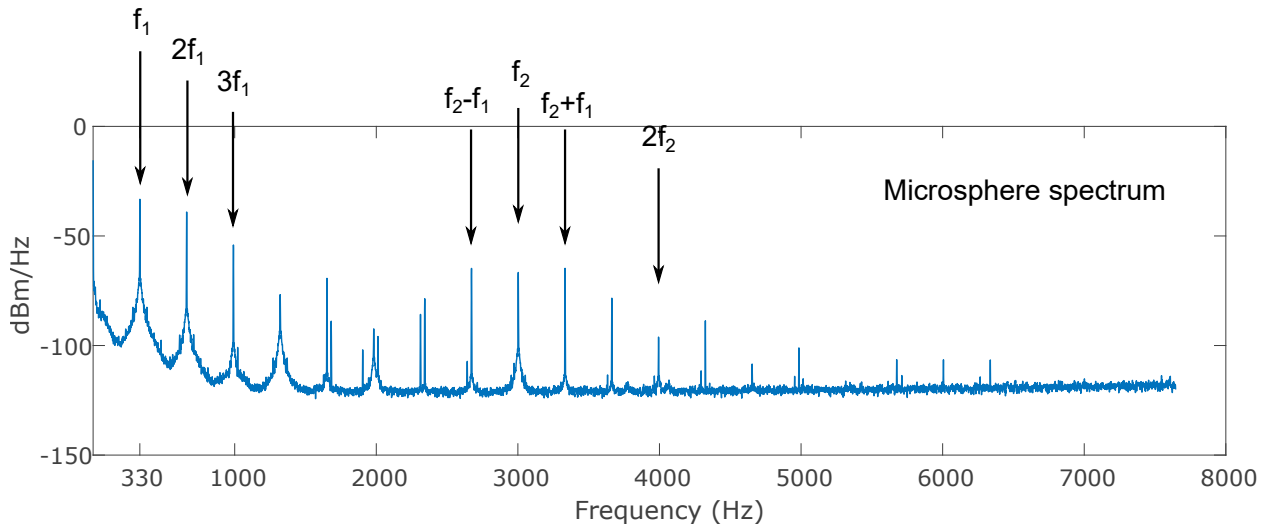

Figure 4.14: PSD of the microsphere motion trapped with the two drive frequencies f_1 and f_2.

Conclusions and outlook

Summary

We have presented the realization and tests of a setup for levitating nanospheres and microspheres, based on an electrodynamic Paul trap. This setup will be the basis for a future optomechanics experiment. This work aimed to demonstrate the feasibility of trapping two particles with a very large charge-to-mass ratio difference, by means of a two-frequency electric field.

We have first illustrated how a test linear Paul trap was designed and fabricated. Then, the methods used to charge and load the different particles inside the trap were shown.

We then proceeded to characterize the working trap. Two main procedures were used to measure the charge-to-mass ratio of trapped particles: one direct, by means of measuring the particle equilibrium position within the electric fields of the trap and extracting the ratio from computer simulations, and one indirect, by fitting the measured stable regions of the trap operation to the theoretical prediction. With these methods, we were able to reconstruct the charge-to-mass distribution resulting from two different launching techniques, and to find a main difference between nanosphere and microsphere of $(Q/m)_n/(Q/m)_\mu \sim 10^3$. Afterwards, we have shown how the interferometric detection system measurements revealed the overdamped regime of the trapped particles.

Finally, we tried to use the two frequency approach to simultaneously trap nano and microsphere. Here, however, we came up against the limits of our system, namely, both the high air damping felt by the nanosphere and the limitations of our voltage and frequency supplies with regards to the accessible parameter space. As a result, within our accessible experiment regimes, the second field was found to be unnecessary for trapping both species. Further investigations will have to remove the effects of air drag by inserting the whole system in a vacuum environment.

Next step: loading nanospheres in vacuum

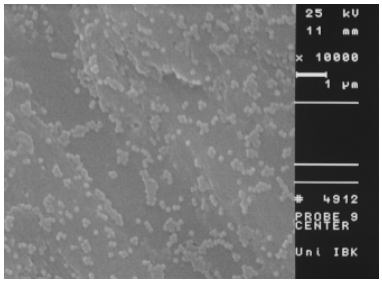

Figure 4.15: Scanning electron microscope image of nanospheres deposited on the aluminum foil.

During the period of my thesis research, other work was being carried our in parallel in the optomechanics laboratory.

A crucial requirement that the new system will have to fulfill is to allow the launching and trapping of nanospheres at the ultra-high vacuum (UHV) level, that is, at $\sim 10^{-10}$ mbar. This is the threshold pressure level that ensures stable operation of a Paul trap with a single trapped calcium ion [82]. Thus, I had the great opportunity to assist in the design and the assembly of the vacuum chamber for testing UHV loading of nanoparticles. Currently, the group is testing laser adsorption loading of nanospheres. This technique consists of a layer of nanosphere solution evaporated on one side of a substrate (a thin metal foil, with thickness from 10 µm to 300 µm), which is placed in vacuum and irradiated by a pulsed laser. The laser can induce an acoustic wave in the substrate, which travels through the material and desorbs the nanospheres on the other side. In this way, a beam of nanospheres is expected to be formed.

This system is now mounted in the vacuum chamber, and as a first preliminary result, we were able to trap

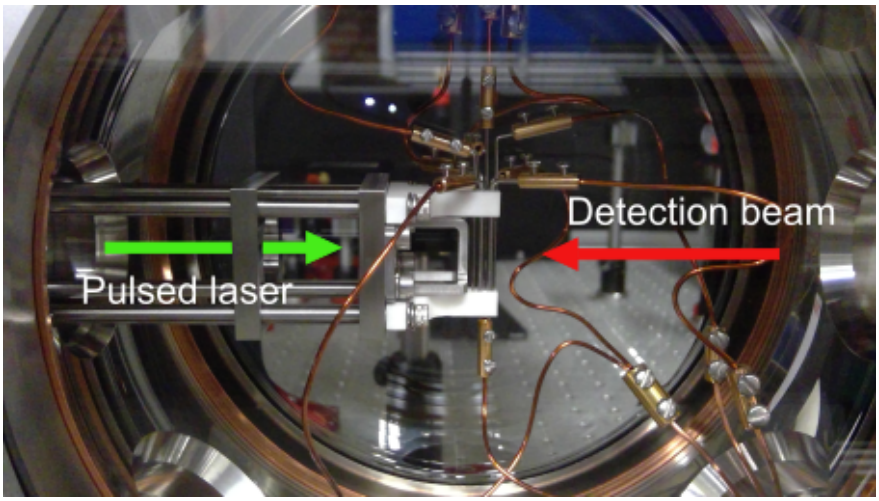

Figure 4.16: Vacuum chamber for testing the ablation loading of nanospheres.

particles down to pressure of $\sim 10^{-5}$ mbar.

Appendices

Appendix A

Numerical code for the stability diagrams

A numerical code for the evaluation of the stability diagrams shown in the main text was written using the software Matlab.

$function\ beta = beta\_p(a, p, q)$

$n = 3;$

$h = 10;$

$d = 2 * h + 2 * (n - 2) + 5;$

$r = (d - 1)/2;$

$A = eye(d) - q. * diag(1./(a - (2 * (-r : r - 1)).^2), 1) - q. * diag(1./(a - (2 * (-r + 1 : r)).^2), -1) - p. * diag(1./(a - (2 * (-r : r - n)).^2), n) - p. * diag(1./(a - (2 * (-r + n : r)).^2), -n);$

$det_A = det(A);$

$if(mod(sqrt(abs(a)), 2) == 0)$

$beta = 1/pi * acos(2 * det(eye(d) - q. * diag(1./(a - (1 + 2 * (-r : r - 1)).^2), 1) - q. * diag(1./(a - (1 + 2 * (-r + 1 : r)).^2), -1) - p. * diag(1./(a - (1 + 2 * (-r : r - n)).^2), n) - p. * diag(1./(a - (1 + 2 * (-r + n : r)).^2), -n)) - 1);$

$else$

$beta = 2/pi * asin(sqrt(det_A * (sin(pi/2. * sqrt(a))^2)));$

end

end

$x = [0 : 0.05 : 50]; \%arange$

$y = [0 : 0.05 : 25]; \%qrange$

$forh = 1 : length(x)$

$forj = 1 : length(y)$

$mat(j, h) = beta\_p(x(h), 0, y(j));$

end

end

$[X, Y] = meshgrid(y, x);$

$figure;$

$[C, r] = contour(X, Y, real(mat'), ' k');$

$w = r.LevelList;$

$r.LevelList = [1, 0.001];$

$holdon$

Bibliography

[1] V. Braginski and A. Manukin, "Ponderomotive effects of electromagnetic radiation," *Sov. Phys. JETP*, vol. 25, no. 4, pp. 653–655, 1967.

[2] B. Abbott et al, "Observation of a kilogram-scale oscillator near its quantum ground state," *New Journal of Physics*, vol. 11, no. 7, p. 073032, 2009.

[3] T. A. Palomaki, J. W. Harlow, J. D. Teufel, R. W. Simmonds, and K. W. Lehnert, "Coherent state transfer between itinerant microwave fields and a mechanical oscillator," *Nature*, vol. 495, p. 210, Mar 2013.

[4] J. Chan, T. P. M. Alegre, A. H. Safavi-Naeini, J. T. Hill, A. Krause, S. Gröblacher, M. Aspelmeyer, and O. Painter, "Laser cooling of a nanomechanical oscillator into its quantum ground state," *Nature*, vol. 478, p. 89, Oct 2011.

[5] T. P. Purdy, D. W. C. Brooks, T. Botter, N. Brahms, Z.-Y. Ma, and D. M. Stamper-Kurn, "Tunable cavity optomechanics with ultracold atoms," *Phys. Rev. Lett.*, vol. 105, p. 133602, Sep 2010.

[6] O. Romero-Isart, A. C. Pflanzer, M. L. Juan, R. Quidant, N. Kiesel, M. Aspelmeyer, and J. I. Cirac, "Optically levitating dielectrics in the quantum regime: Theory and protocols," *Phys. Rev. A*, vol. 83, p. 013803, Jan 2011.

[7] A. C. Pflanzer, O. Romero-Isart, and J. I. Cirac, "Optomechanics assisted by a qubit: From dissipative state preparation to many-partite systems," *Phys. Rev. A*, vol. 88, p. 033804, Sep 2013.

[8] D. Trypogeorgos and C. J. Foot, "Cotrapping different species in ion traps using multiple radio frequencies," *Phys. Rev. A*, vol. 94, p. 023609, Aug 2016.

[9] A. Siegman, *Lasers*. University Science Books, 1986.

[10] C. W. Gardiner and P. Zoller, *Quantum Noise*. Springer, second ed., 2000.

[11] M. Aspelmeyer, T. J. Kippenberg, and F. Marquardt, "Cavity optomechanics," *Rev. Mod. Phys.*, vol. 86, pp. 1391–1452, Dec 2014.

[12] D. E. Chang, C. A. Regal, S. B. Papp, D. J. Wilson, J. Ye, O. Painter, H. J. Kimble, and P. Zoller, "Cavity opto-mechanics using an optically levitated nanosphere," *Proceedings of the National Academy of Sciences*, vol. 107, no. 3, pp. 1005–1010, 2010.

[13] J. Millen, P. Z. G. Fonseca, T. Mavrogordatos, T. S. Monteiro, and P. F. Barker, "Cavity cooling a single charged levitated nanosphere," *Phys. Rev. Lett.*, vol. 114, p. 123602, Mar 2015.

[14] J. Schwinger, *The Theory of Obstacles in Resonant Cavities and Wave Guides*. Report (Massachusetts Institute of Technology. Radiation Laboratory), Radiation Laboratory, Massachusetts Institute of Technology, 1943.

[15] L. Novotny and B. Hecht, *Principles of Nano-Optics*. Cambridge University Press, 2 ed., 2012.

[16] A. A. Clerk and F. Marquardt, *Basic Theory of Cavity Optomechanics*, pp. 5–23. Berlin, Heidelberg: Springer Berlin Heidelberg, 2014.

[17] J. Gieseler, B. Deutsch, R. Quidant, and L. Novotny, "Subkelvin parametric feedback cooling of a laser-trapped nanoparticle," *Phys. Rev. Lett.*, vol. 109, p. 103603, Sep 2012.

[18] N. Kiesel, F. Blaser, U. Delić, D. Grass, R. Kaltenbaek, and M. Aspelmeyer, "Cavity cooling of an optically levitated submicron particle," *Proceedings of the National Academy of Sciences*, vol. 110, no. 35, pp. 14180–14185, 2013.

[19] T. S. Monteiro, J. Millen, G. A. T. Pender, F. Marquardt, D. Chang, and P. F. Barker, "Dynamics of levitated nanospheres: towards the strong coupling regime," *New Journal of Physics*, vol. 15, no. 1, p. 015001, 2013.

[20] J.-M. Pirkkalainen, S. U. Cho, F. Massel, J. Tuorila, T. T. Heikkilä, P. J. Hakonen, and M. A. Sillanpää, "Cavity optomechanics mediated by a quantum two-level system," *Nature Communications*, vol. 6, p. 6981, Apr 2015.

[21] A. B. Mundt, A. Kreuter, C. Becher, D. Leibfried, J. Eschner, F. Schmidt-Kaler, and R. Blatt, "Coupling a single atomic quantum bit to a high finesse optical cavity," *Phys. Rev. Lett.*, vol. 89, p. 103001, Aug 2002.

[22] A. Stute, B. Casabone, P. Schindler, T. Monz, P. O. Schmidt, T. E. Northup, and R. Blatt, "Tunable ion-photon entanglement in an optical cavity," *Nature*, vol. 485, p. 482, May 2012.

[23] E. T. Jaynes and F. W. Cummings, "Comparison of quantum and semiclassical radiation theories with application to the beam maser," *Proceedings of the IEEE*, vol. 51, no. 1, pp. 89–109, 1963.

[24] S. Haroche and J.-M. Raimond, *Exploring the quantum: atoms, cavities, and photons*. Oxford University press, 2006.

[25] C. K. Law and J. H. Eberly, "Arbitrary control of a quantum electromagnetic field," *Phys. Rev. Lett.*, vol. 76, pp. 1055–1058, Feb 1996.

[26] W. Paul, "Electromagnetic traps for charged and neutral particles," *Rev. Mod. Phys.*, vol. 62, pp. 531–540, Jul 1990.

[27] S. I. Kopnin, T. I. Morozova, and S. I. Popel, "Electron beam action and high charging of dust particles," *IEEE Transactions on Plasma Science*, vol. PP, no. 99, pp. 1–3, 2017.

[28] S. Schlemmer, J. Illemann, S. Wellert, and D. Gerlich, "Nondestructive high-resolution and absolute mass determination of single charged particles in a three-dimensional quadrupole trap," *Journal of Applied Physics*, vol. 90, no. 10, pp. 5410–5418, 2001.

[29] C. J. Foot, D. Trypogeorgos, E. Bentine, A. Gardner, and M. Keller, "Two-frequency operation of a Paul trap to optimise confinement of two species of ions," *arXiv:1801.00424*, 2018.

[30] D. Leibfried, R. Blatt, C. Monroe, and D. Wineland, "Quantum dynamics of single trapped ions," *Rev. Mod. Phys.*, vol. 75, pp. 281–324, Mar 2003.

[31] P. Ghosh, *Ion Traps*. Clarendon Press, 1995.

[32] M. Abramowitz, *Handbook of Mathematical Functions, With Formulas, Graphs, and Mathematical Tables*. Dover Publications, Incorporated, 1974.

[33] "Dynamical stability of a pendulum when its point of suspension vibrates," in *Collected Papers of P.L. Kapitza* (D. T. Haar, ed.), pp. 714 – 725, Pergamon, 1965.

[34] L. D. Landau and E. M. Lifshitz, *Mechanics*. Pergamon Press: Oxford, 1969.

[35] H. C. Nägerl, C. Roos, D. Leibfried, H. Rohde, G. Thalhammer, J. Eschner, F. Schmidt-Kaler, and R. Blatt, "Investigating a qubit candidate: Spectroscopy on the $S_{1/2}$ to $D_{5/2}$ transition of a trapped calcium ion in a linear Paul trap," *Phys. Rev. A*, vol. 61, p. 023405, Jan 2000.

[36] S. R. Jefferts, C. Monroe, A. S. Barton, and D. J. Wineland, "Paul trap for optical frequency standards," *IEEE Transactions on Instrumentation and Measurement*, vol. 44, pp. 148–150, April 1995.

[37] R. Alheit, S. Kleineidam, F. Vedel, M. Vedel, and G. Werth, "Higher order non-linear resonances in a Paul trap," *International Journal of Mass Spectrometry and Ion Processes*, vol. 154, no. 3, pp. 155 – 169, 1996.

[38] W. M. Itano and D. J. Wineland, "Laser cooling of ions stored in harmonic and penning traps," *Phys. Rev. A*, vol. 25, pp. 35–54, Jan 1982.

[39] F. G. Major and H. G. Dehmelt, "Exchange-collision technique for the rf spectroscopy of stored ions," *Phys. Rev.*, vol. 170, pp. 91–107, Jun 1968.

[40] T. Li, S. Kheifets, and M. G. Raizen, "Millikelvin cooling of an optically trapped microsphere in vacuum," *Nature Physics*, vol. 7, p. 527 EP, Mar 2011.

[41] V. Jain, J. Gieseler, C. Moritz, C. Dellago, R. Quidant, and L. Novotny, "Direct measurement of photon recoil from a levitated nanoparticle," *Phys. Rev. Lett.*, vol. 116, p. 243601, Jun 2016.

[42] N. McLachlan, *Theory and application of Mathieu functions*. Clarendon Press, 1947.

[43] T. Hasegawa and K. Uehara, "Dynamics of a single particle in a Paul trap in the presence of the damping force," *Applied Physics B*, vol. 61, pp. 159–163, Aug 1995.

[44] N. V. Konenkov, M. Sudakov, and D. J. Douglas, "Matrix methods for the calculation of stability diagrams in quadrupole mass spectrometry," *Journal of the American Society for Mass Spectrometry*, vol. 13, pp. 597–613, Jun 2002.

[45] X. Chu, M. Holzki, R. Alheit, and G. Weitha, "Observation of high-order motional resonances of an ion cloud in a Paul trap," *International Journal of Mass Spectrometry and Ion Processes*, vol. 173, no. 1, pp. 107 – 112, 1998.

[46] M. A. N. Razvi, X. Z. Chu, R. Alheit, G. Werth, and R. Blümel, "Fractional frequency collective parametric resonances of an ion cloud in a Paul trap," *Phys. Rev. A*, vol. 58, pp. R34–R37, Jul 1998.

[47] X. Zhao, V. L. Ryjkov, and H. A. Schuessler, "Parametric excitations of trapped ions in a linear rf ion trap," *Phys. Rev. A*, vol. 66, p. 063414, Dec 2002.

[48] N. Leefer, K. Krimmel, W. Bertsche, D. Budker, J. Fajans, R. Folman, H. Häffner, and F. Schmidt-Kaler, "Investigation of two-frequency Paul traps for antihydrogen production," *Hyperfine Interactions*, vol. 238, p. 12, Dec 2016.

[49] D. J. Larson, J. C. Bergquist, J. J. Bollinger, W. M. Itano, and D. J. Wineland, "Sympathetic cooling of trapped ions: A laser-cooled two-species nonneutral ion plasma," *Phys. Rev. Lett.*, vol. 57, pp. 70–73, Jul 1986.

[50] D. Offenberg, C. B. Zhang, C. Wellers, B. Roth, and S. Schiller, "Translational cooling and storage of protonated proteins in an ion trap at subkelvin temperatures," *Phys. Rev. A*, vol. 78, p. 061401, Dec 2008.

[51] A. Ashkin, J. M. Dziedzic, J. E. Bjorkholm, and S. Chu, "Observation of a single-beam gradient force optical trap for dielectric particles," *Opt. Lett.*, vol. 11, pp. 288–290, May 1986.

[52] M. Nasse and C. Foot, "Influence of background pressure on the stability region of a Paul trap," *European Journal of Physics*, vol. 22, no. 6, p. 563, 2001.

[53] W. Guan, S. Joseph, J. H. Park, P. S. Krstić, and M. A. Reed, "Paul trapping of charged particles in aqueous solution," *Proceedings of the National Academy of Sciences*, vol. 108, no. 23, pp. 9326–9330, 2011.

[54] C. E. Pearson, D. R. Leibrandt, W. S. Bakr, W. J. Mallard, K. R. Brown, and I. L. Chuang, "Experimental investigation of planar ion traps," *Phys. Rev. A*, vol. 73, p. 032307, Mar 2006.

[55] S. T. Gulde, *Experimental Realization of Quantum Gates and the Deutsch-Jozsa Algorithm with Trapped calcium ions*. PhD thesis, Universitat Innsbruck, 2003.

[56] M. Raizen, J. Gilligan, J. C. Bergquist, W. Itano, and D. J. Wineland, "Ionic crystals in a linear Paul trap," vol. 45, pp. 6493–6501, 06 1992.

[57] H. Dehmelt, "Radiofrequency spectroscopy of stored ions i: Storage," vol. 3 of *Advances in Atomic and Molecular Physics*, pp. 53 – 72, Academic Press, 1968.

[58] D. R. Denison, "Operating parameters of a quadrupole in a grounded cylindrical housing," *Journal of Vacuum Science and Technology*, vol. 8, no. 1, pp. 266–269, 1971.

[59] Idemat, "Electrical properties of pom," 2003.

[60] R. B. Cole, "Some tenets pertaining to electrospray ionization mass spectrometry," *Journal of Mass Spectrometry*, vol. 35, no. 7, pp. 763–772, 2000.

[61] R. L. Grimm and J. L. Beauchamp, "Evaporation and discharge dynamics of highly charged multicomponent droplets generated by electrospray ionization," *The Journal of Physical Chemistry A*, vol. 114, no. 3, pp. 1411–1419, 2010. PMID: 19848399.

[62] "Disintegration of water drops in an electric field," *Proceedings of the Royal Society of London A: Mathematical, Physical and Engineering Sciences*, vol. 280, no. 1382, pp. 383–397, 1964.

[63] "Studies in electrohydrodynamics. i. the circulation produced in a drop by an electric field," *Proceedings of the Royal Society of London A: Mathematical, Physical and Engineering Sciences*, vol. 291, no. 1425, pp. 159–166, 1966.

[64] K. Visscher, S. P. Gross, and S. M. Block, "Construction of multiple-beam optical traps with nanometer-resolution position sensing," *IEEE Journal of Selected Topics in Quantum Electronics*, vol. 2, pp. 1066–1076, Dec 1996.

[65] J. H. G. Huisstede, K. O. van der Werf, M. L. Bennink, and V. Subramaniam, "Force detection in optical tweezers using backscattered light," *Opt. Express*, vol. 13, pp. 1113–1123, Feb 2005.

[66] A. Pralle, M. Prummer, E.-L. Florin, E. Stelzer, and J. Hörber, "Three-dimensional high-resolution particle tracking for optical tweezers by forward scattered light," *Microscopy Research and Technique*, vol. 44, no. 5, pp. 378–386, 1999.

[67] M. W. Allersma, F. Gittes, M. J. deCastro, R. J. Stewart, and C. F. Schmidt, "Two-dimensional tracking of ncd motility by back focal plane interferometry," *Biophysical Journal*, vol. 74, no. 2, pp. 1074 – 1085, 1998.

[68] S. F. Tolić-Nørrelykke, E. Schäffer, J. Howard, F. S. Pavone, F. Jülicher, and H. Flyvbjerg, "Calibration of optical tweezers with positional detection in the back focal plane," *Review of Scientific Instruments*, vol. 77, no. 10, p. 103101, 2006.

[69] F. Gittes and C. F. Schmidt, "Interference model for back-focal-plane displacement detection in optical tweezers," *Opt. Lett.*, vol. 23, pp. 7–9, Jan 1998.

[70] J. Jackson, *Classical Electrodynamics*. Wiley, 2007.

[71] P. Mestres Junque, *Cavity optomechanics with optically trapped particles*. PhD thesis, Universitat Politecnica de Catalunya, 2017.

[72] J. W Shaevitz, "A practical guide to optical trapping,"

[73] "What is pyrpl?." `http://pyrpl.readthedocs.io/en/latest/index.html`.

[74] C. R. Howder, D. M. Bell, and S. L. Anderson, "Optically detected, single nanoparticle mass spectrometer with pre-filtered electrospray nanoparticle source," *The Review of scientific instruments*, vol. 85, p. 014104, January 2014.

[75] A. Kuhlicke, A. Rylke, and O. Benson, "On-demand electrostatic coupling of individual precharacterized nano- and microparticles in a segmented Paul trap," *Nano Letters*, vol. 15, no. 3, pp. 1993–2000, 2015. PMID: 25688754.

[76] S. A. Beresnev, V. G. Chernyak, and G. A. Fomyagin, "Motion of a spherical particle in a rarefied gas. part 2. drag and thermal polarization," *Journal of Fluid Mechanics*, vol. 219, p. 405–421, 1990.

[77] M. C. Wang and G. E. Uhlenbeck, "On the theory of the brownian motion ii," *Rev. Mod. Phys.*, vol. 17, pp. 323–342, Apr 1945.

[78] R. Blatt, P. Zoller, G. Holzmüller, and I. Siemers, "Brownian motion of a parametric oscillator: A model for ion confinement in radio frequency traps," *Zeitschrift für Physik D Atoms, Molecules and Clusters*, vol. 4, pp. 121–126, Jun 1986.

[79] R. Kubo, "The fluctuation-dissipation theorem," *Reports on Progress in Physics*, vol. 29, no. 1, p. 255, 1966.

[80] M. Madsen, W. Hensinger, D. Stick, J. Rabchuk, and C. Monroe, "Planar ion trap geometry for microfabrication," *Applied Physics B*, vol. 78, pp. 639–651, Mar 2004.

[81] J. Chiaverini, R. B. Blakestad, J. Britton, J. D. Jost, C. Langer, D. Leibfried, R. Ozeri, and D. J. Wineland, "Surface-electrode architecture for ion-trap quantum information processing," *Quantum Info. Comput.*, vol. 5, pp. 419–439, Sept. 2005.

[82] C. F. Roos, *Controlling the quantum state of trapped ions.* PhD thesis, Universitat Innsbruck, 2000.